

Sensitivity analysis of attenuation in convective rainfall at X-Band frequency using the Mountain Reference Technique

Guy Delrieu, Anil Kumar Khanal, Frédéric Cazenave, and Brice Boudevillain

HMCIS Team, Institute for Geosciences and Environmental research (IGE),
UMR 5001 (Université Grenoble Alpes, CNRS, IRD, Grenoble-INP), Grenoble, France

Abstract. The RadAlp experiment aims at improving quantitative precipitation estimation (QPE) in the Alps thanks to X-band polarimetric radars and in-situ measurements deployed in the region of Grenoble, France. In this article, we revisit the physics of propagation and attenuation of microwaves in rain. We first derive four attenuation – reflectivity (AZ) algorithms constrained or not by path-integrated attenuations (PIA) estimated from the decrease in return of selected mountain targets when it rains compared to their dry-weather levels (the so-called Mountain Reference Technique - MRT). We also consider one simple polarimetric algorithm based on the profile of the total differential phase shift between the radar and the mountain targets. The central idea of the work is to implement these five algorithms all together in the framework of a generalized sensitivity analysis in order to establish useful parameterizations for QPE-attenuation correction. The parameter structure and the inherent mathematical ambiguity of the system of equations make it necessary to organize the optimization procedure in a nested way. The core of the procedure consists in (i) exploring with classical sampling techniques the space of the parameters allowed to be variable from one target to the other and from one time-step to the next, (ii) computing a cost function (CF) quantifying the proximity of the simulated profiles and (iii) selecting parameters sets for which a given CF threshold is exceeded. This core is activated for a series of values of parameters supposed to be fixed, e.g. the radar calibration error for a given event. The sensitivity analysis is performed for a set of three convective events using the 0°-elevation PPI measurements of the Météo-France weather radar located on top of the Moucherotte Mount (altitude of 1901 m asl). It allows the estimation of critical parameters for radar QPE using radar data alone. In addition to the radar calibration error, this includes time series of radome attenuation and estimations of the coefficients of the power-law models relating the specific attenuation and the reflectivity (A-Z relationship) on the one hand and the specific attenuation and the specific differential phase shift (A-K_{dp} relationship) on the other hand. It is noteworthy that the A-Z and A-K_{dp} relationships obtained are consistent with those derived from concomitant drop size distribution measurements at ground level, in particular with a slightly non-linear A-K_{dp} relationship ($A = 0.275 K_{dp}^{1.1} + 28 K_{dp}^{1.1}$). X-Band radome attenuations as high as 15 dB were estimated, leading to the recommendation of avoiding the use of radomes for remote sensing of precipitation at such frequency.

Correspondence to: guy.delrieu@univ-grenoble-alpes.fr

Mis en forme : Police :Non Italique

Mis en forme : Police :Non Italique

Mis en forme : Police :Non Italique

Mis en forme : Police :Non Italique

Mis en forme : Police :Non Italique

Mis en forme : Police :Non Italique

Mis en forme : Police :Non Italique

1. Introduction

Estimation of atmospheric precipitation is important in a high mountain region such as the Alps for the assessment and management of water and snow resources (drinking water, hydro-power production, agriculture and tourism) as well as for prediction of natural hazards associated with intense precipitation and snowpack melting. In complement with in-situ raingauge networks and snowpack monitoring systems, remote sensing using ground-based weather radar systems has a high potential that needs to be exploited but also a number of several limitations that need to be surpassed. A first dilemma is related to the choice of the altitude of the radar setup with a compromise to be found between maximizing the visibility of the radar system(s) at the regional scale and increasing the representativeness of the measurements made in altitude with respect compared to precipitation reaching the ground, especially during cold periods. A second dilemma is the well-known detection / resolution versus attenuation compromise, which is acute for weather radar frequencies. S-Band and C-Band frequencies (around 3 and 5 GHz, respectively) are traditionally preferred in continental-wide weather radar networks (Serafin and Wilson, 2000; Saxion et al. 2011, Saltikoff et al. 2019) for their appropriate precipitation detection capability and their moderate sensitivity to attenuation. In Europe, MétéoSwiss has the longest-standing experience in operating such a C-Band weather radar network in high-mountain regions (Joss and Lee, 1995; Germann et al. 2006; Sideris et al. 2014; Foresti et al. 2018). Implementation of radars operating at the X-Band frequency (~9-10 GHz) has also been proposed in the last decades for research and operational applications at local scales, e.g., for precipitation monitoring in urban areas and/or in mountainous regions (Delrieu et al. 1997; McLaughlin et al. 2009; Scipion et al. 2013; Lengfeld et al. 2014, to name just a few). The renewed interest for in the X-Band frequency, known for long to be prone to attenuation (e.g., Hirschfeld and Bordan 1954), is based on the promises of polarimetric techniques (e.g. Bringi and Chandrasekar 2001; Ryzhkov et al. 2005) for attenuation correction (Testud et al. 2000; Matrosov and Clark, 2002; Matrosov et al. 2005; Matrosov et al. 2009; Koffi et al. 2014, Ryzhkov et al. 2014). Météo-France has chosen to complement the coverage of its operational radar network ARAMIS (for Application Radar à la Météorologie Infra-Synoptique) in the Alps by means of X-Band polarimetric radars. A first set of three radars was installed in Southern Alps within the RHvTMME project (Risques Hydrométéorologiques en Territoires de Montagnes et Méditerranéens) in the period 2008-2013 (Westrelin et al. 2012; Yu et al. 2018). An additional radar (MOUC radar, hereinafter) was installed in 2014 on top of the Mount Moucherotte (1901 m) that dominates oversees the valley of Grenoble. The RadAlp experiment (Khanal et al. 2019; Delrieu et al. 2020) is a contribution to research aimed at improving quantitative precipitation estimation (QPE) based on the Météo France MOUC radar, complemented by a suite of sensors installed on the Grenoble valley floor at the Institute for Geosciences and Environmental research (IGE, 210 m asl). This includes the IGE research X-Band polarimetric radar named XPORT, a K-Band Micro Rain Radar (MRR) and in-situ sensors (disdrometers, raingauges).

The present article aims to show that mountain returns can be useful for the parameterisation of QPE algorithms for weather radar systems operating at attenuating frequencies in mountainous regions. It is part of a series of contributions devoted to the Surface Reference Technique proposed for spaceborne radar configuration (Meneghini et al. 1983; Marzoug and Amayenc, 1994; and more recently Meneghini et al. 2020) and its transposition to ground-based radar configurations with the Mountain

Mis en forme : Police :Non Italique

Mis en forme : Police :Non Italique

Mis en forme : Police :Non Italique

65 Reference Technique (Delrieu et al. 1997, Serrar et al. 2000, Delrieu et al. 2020). Figures 1 and 2 illustrate our point. Figure 1 shows a map of dry-weather mountain returns of the MOUC radar. The configuration of the radars operated in the RadAlp experiment is recalled in the insert; note that only the MOUC radar data is used in the current study. The measurements are taken at an elevation angle of 0° which corresponds to the lowest PPI of the volume-scanning strategy of the MOUC radar. The reflectivity data are averaged over a ~~four-hour period of four hours~~; one PPI is performed at the 0° -elevation angle every
70 five minutes. We have selected 22 mountain targets corresponding to compact groups of gates in successive radials (3-6 typically; the radial spacing is 0.5°) and ranges (5-10 gates; the gate extent is 240 m) presenting a majority of dry-weather reflectivity values greater than 45 dBZ. The paths between the radar and the targets are free of beam blockages and present as few noisy gates (due to side lobes) as possible. In addition to the reflectivity map, the top graphs of Fig. 2 display the co-polar correlation ($\rho_{\text{HH}}\rho_{\text{HV}}$) and the total differential phase shift ($\Psi_{\text{ZH}}\Psi_{\text{ZD}}$) maps at 14:15:00 UTC on 21 July 2017 before the convective
75 event that occurred that day between 15:30 and 18:00 UTC. The $\Psi_{\text{ZH}}\Psi_{\text{ZD}}$ map is essentially noisy at that time and the red colour in the $\rho_{\text{HH}}\rho_{\text{HV}}$ map, corresponding to values close to 1, highlights some small rain cells, in particular one in the south of the radar domain close to Target 22 (Grand Veymont Mount). The middle row maps correspond to the occurrence of intense precipitation over the city of Grenoble at 16:05 UTC. A peak of 40 mm h^{-1} in ten minutes was recorded at that time by the rain gauge located on top of the IGE building. The $\Psi_{\text{ZH}}\Psi_{\text{ZD}}$ map displays marked increasing radial profiles in the North-East
80 (NE) direction. The $\rho_{\text{HH}}\rho_{\text{HV}}$ map allows a good delimitation of the whole rain pattern and clearly shows the dominance of the mountain returns over the rain returns for most of the Belledonne and Taillefer targets. The most striking observation on the reflectivity map is the dramatic decrease of the mountain returns of Targets 1-10 in the NE sector which results with no doubt from the rain cell falling over the city of Grenoble at that time. This is a clear example of what will be termed as “along-path attenuation” hereinafter. On the bottom row of Fig. 2, which corresponds to the measurements made at 17:00 UTC, one can
85 observe a similar strong along-path attenuation in the NE direction in the $\Psi_{\text{ZH}}\Psi_{\text{ZD}}$ map, associated with a second 40 mm h^{-1} rainrate peak at the IGE site (see eventually the hyetograph in Delrieu et al. (2020), their Fig. 2). But more impressive is the general decrease of returns from all the mountain targets, associated with a rain cell occurring at the radar site. This is an example of so-called “on-site attenuation”, related to the formation of a water film on the radome, combined with along-path attenuation in the immediate vicinity of the radar site.

90

The article is organised as follows. In the theoretical part (section 2), we find [it](#) useful to revisit in some detail the physics of propagation and attenuation of microwaves in rain. We derive (section 2.2) four attenuation – reflectivity (AZ) algorithms constrained or not by path-integrated attenuations (PIA) estimated from the decrease in return of selected mountain targets when it rains, compared to their dry-weather levels. We also consider [onea](#) simple polarimetric algorithm based on the profile
95 of the total differential phase shift between the radar and the mountain targets (section 2.3). The structure and interdependencies of the parameters are discussed in section 2.4. This leads to the description of the principles of the generalized sensitivity

analysis proposed for studying the physical model at hand (section 3.1). The results obtained are illustrated and discussed item by item in sub-sections 3.2.1-3.2.5. Concluding remarks and future work are presented in section 4.

2. Theory

100

2.1 Basic definitions and notations

Let us express the radar returned power profile $P(r)$ [mW] as:

$$P(r) = \frac{C}{r^2} Z(r) AF(r) \quad (2.1)$$

105

where $Z(r)$ [$\text{mm}^6 \text{m}^{-3}$] is the true reflectivity profile, $AF(r)$ [-] is the attenuation factor at range r [km] and C is the radar constant. We suppose the measured reflectivity profile $Z_m(r)$ to depend both on the attenuation and on a possible radar calibration error denoted dC :

$$Z_m(r) = \frac{P(r) r^2}{C} = Z(r) AF(r) dC \quad (2.2)$$

110

In addition to the running range r , let us consider the range r_0 corresponding to the blind range of the radar system, eventually extended to the range where the reflectivity measurements start to be free of spurious detections due e.g. to side lobes.

The attenuation factor $AF(r)$ is expressed as the product of two terms:

$$AF(r) = AF(r_0) AF(r, r_0) \quad (2.3)$$

115

where $AF(r_0)$ is the on-site attenuation factor which, as discussed in the introduction, may result from two main sources: attenuation due to a water film on the radome and along-path attenuation due to precipitation falling between the radar site and range r_0 .

As a classical formulation (e.g. Marzoug and Amayenc, 1994), we express the two-way attenuation factor as a function of the specific attenuation profile $A(r)$ [dB km^{-1}] through the following equation:

120

$$AF(r) = AF(r_0) \exp\left(-0.46 \int_{r_0}^r A(s) ds\right) \quad (2.4)$$

Mis en forme : Police :Non Italique

Mis en forme : Police :Non Italique

To go further, we have to introduce relationships between the radar measurables (specific attenuation and reflectivity) and the variable of interest for QPE, i.e. the rainrate R [mm h^{-1}], which are assumed to be of power type with the following notations:

$$A = a_{AZ} Z^{b_{AZ}} \quad (2.5)$$

$$R = a_{RA} A^{b_{RA}} \quad (2.6)$$

$$R = a_{RZ} Z^{b_{RZ}} \quad (2.7)$$

The order used for the variables in equations 2.5-2.7 is meaningful since the specific attenuation profile is derived from the measured reflectivity profile, while the rainrate profile can be derived in a second step either from the specific attenuation profile or from the corrected reflectivity profile. Due to the well-known lower variability of the R-A relationship compared to the R-Z relationship, (2.6) should be preferred to (2.7) for the estimation of the rainrate profiles (Ryzhkov et al. 2014).

Let us now consider another particular range, denoted r_m , where estimates of the attenuation factor may be available. We use the following notation:

$$AF(r_m) = AF(r_m) dAF_m AF_m(r_m) = AF(r_m) dAF_m \quad (2.8)$$

where $AF(r_m)$ is the true attenuation factor at range r_m and the term dAF_m represents a multiplicative error term. As illustrated in the introduction, such direct estimates of the attenuation factor can be obtained in mountainous regions from using the MRT.

We frequently use hereinafter the notion of path-integrated attenuation (PIA), in units of dB, defined as:

$$PIA(r) = -10 \log_{10}(AF(r)) \quad (2.9)$$

Note that since $AF(r)$ is comprised between 1 (no attenuation) and 0 (full attenuation), the PIA subsequently takes values in the range of 0 (no attenuation) up to $+\infty$ (full attenuation). The PIAs at ranges r_0 and r_m are denoted PIA_0 and PIA_m , respectively, in the following.

Mis en forme : Police :Non Italique

Mis en forme : Police :Non Italique

Mis en forme : Police :Non Italique

155 **2.2 Formulation of the attenuation-reflectivity algorithms**

The following mathematical developments are inspired by the works on rain-profiling algorithms in satellite measurement configuration (e.g., Meneghini et al. 1983; Marzoug, Amayenc 1994). The attenuation-reflectivity algorithms (A-Z algorithms) proposed in this section rely on two basic equations. The first one is the analytical solution of (2.4) when the power-law model (2.5) is supposed to represent perfectly the A-Z relationship. By taking the derivative of $AF^{b_{AZ}}(r_0, r)$ with respect to range r , one obtains:

$$\frac{d(AF^{b_{AZ}}(r_0, r))/dr = AF^{b_{AZ}}(r_0, r) \frac{d(AF^{b_{AZ}}(r_0, r))}{dr} = AF^{b_{AZ}}(r_0, r) (-0.46 \alpha_{AZ} b_{AZ} Z(r)^{b_{AZ}} \alpha_{AZ} b_{AZ} Z(r)^{b_{AZ}}) \quad (2.10)$$

165 Substitution of the true reflectivity by the measured reflectivity through (2.2) and integration between r_0 and r yields:

$$AF^{b_{AZ}}(r_0, r) AF^{b_{AZ}}(r_0, r) = 1 - 0.46 \alpha_{AZ} b_{AZ} SZ(r_0, r) \alpha_{AZ} b_{AZ} SZ(r_0, r) / (AF(r_0) dC)^{b_{AZ}} / (AF(r_0) dC)^{b_{AZ}}$$

170 with:

$$SZ(r_0, r) = \int_{r_0}^r Z_m(s)^{b_{AZ}} ds \quad (2.11)$$

$$SZ(r_0, r) = \int_{r_0}^r Z_m(s)^{b_{AZ}} ds$$

175 The second equation is obtained by integrating (2.10) up to range r_m and by introducing the attenuation factor estimate available at this range, yielding:

$$(AF(r_m) / AF(r_0))^{b_{AZ}} (AF(r_m) / AF(r_0))^{b_{AZ}} + 0.46 \alpha_{AZ} b_{AZ} SZ(r_0, r_m) \alpha_{AZ} b_{AZ} SZ(r_0, r_m) / (AF(r_0) dC)^{b_{AZ}} / (AF(r_0) dC)^{b_{AZ}} = 1 \quad (2.12)$$

185 We develop in the next sub-section Appendix A four formulations of attenuation corrections for a supposedly homogeneous precipitation type, i.e. we assume the α_{AZ} and b_{AZ} coefficients to be constant along the propagation path. Each formulation filters out one of the four parameters α_{AZ} , dC , $AF(r_0)$ and $AF(r_m)$: PIA_m, dC , α_{AZ} and PIA₀, respectively. Note that due to the mathematical expression of the intervening equations there is no possibility to filter out the b_{AZ} parameter, which will be assumed to be constant, close to a value of 0.8 (Ryzkhoverat X-Band (Ryzhkov et al. 2014), and to present a low

Mis en forme : Police :Non Italique

Mis en forme : Police :Non Italique

Mis en forme : Police :Non Italique

Mis en forme : Police :Non Italique

sensitivity in the system of equations. The resulting expressions of the reflectivity and specific attenuation corrected profiles are listed hereafter:

2.2.1 AZhb algorithm (independent of PIA_m):

This formulation is based on (2.11) only. In other words, it does not make use of PIA_m . By combining (2.11), (2.2) and (2.3), one obtains a corrected reflectivity profile through the following equation:

$$Z_{AZhb}(r) = Z_m(r) / [(AF(r_0) dC)^{b_{AZ}} - 0.46 a_{AZ} b_{AZ} SZ(r_0, r)]^{1/b_{AZ}} \quad (2.13)$$

$$Z_{AZhb}(r) = Z_m(r) / [(AF(r_0) dC)^{b_{AZ}} - 0.46 a_{AZ} b_{AZ} SZ(r_0, r)]^{1/b_{AZ}} \quad (2.13)$$

$A_{AZhb}(r) = a_{AZ} Z_m^{b_{AZ}}(r) / [(AF(r_0) dC)^{b_{AZ}} - 0.46 a_{AZ} b_{AZ} SZ(r_0, r)]$ The specific attenuation profile follows from the use of the A-Z power law model (2.5):

$$A_{AZhb}(r) = a_{AZ} Z_m^{b_{AZ}}(r) / [(AF(r_0) dC)^{b_{AZ}} - 0.46 a_{AZ} b_{AZ} SZ(r_0, r)] \quad (2.14)$$

This formulation is equivalent to the solution proposed early by Hitschfeld and Bordan (1954), hence the proposed name AZhb. It can be termed as a “forward algorithm” since only the measured reflectivities between range r_0 and the running range r are used for the correction at range r . The minus sign between the two terms of the denominator indicates that the denominator is not prevented to tend towards 0 when the SZ cumulative term increases. This solution is subsequently known to be unstable and highly sensitive to calibration error, to inadequate values of the A-Z relationship coefficients and to on-site attenuation.

2.2.2 AZC algorithm (independent of dC):

The attenuation constraint (2.11) is now used to express dC as:

$$dC = [0.46 a_{AZ} b_{AZ} SZ(r_0, r_m) / (AF(r_0)^{b_{AZ}} - AF_m(r_m)^{b_{AZ}})]^{1/b_{AZ}} \quad (2.15)$$

which is introduced in (2.11) to yield:

$$AF_{AZC}^{b_{AZ}}(r_0, r) = [AF(r_0)^{b_{AZ}} SZ(r, r_m) + AF(r_m)^{b_{AZ}} SZ(r_0, r)] / AF(r_0)^{b_{AZ}} SZ(r_0, r_m) \quad (2.16)$$

Mis en forme : Police :Non Italique

Mis en forme : Police :Non Italique

Mis en forme : Police :Non Italique

Mis en forme : Police :Non Italique

Mis en forme : Police :Non Italique

Mis en forme : Police :Non Italique

Mis en forme : Police :Non Italique

Mis en forme : Police :Non Italique

Mis en forme : Police :Non Italique

220 The corrected reflectivity profile is then derived from (2.2), (2.3), (2.15) and (2.16) to read as:

$$Z_{AZC}(r) = Z_m(r) [AF(r_0)^{b_{AZ}} - AF(r_m)^{b_{AZ}}]^{1/b_{AZ}} / \{0.46 a_{AZ} b_{AZ} [AF(r_0)^{b_{AZ}} SZ(r, r_m) + AF(r_m)^{b_{AZ}} SZ(r_0, r)]\}^{1/b_{AZ}} \quad (2.17)$$

225 Note that in the previous derivations, the expression of dC given by (2.15) is used two times, first in the expression of $AF_{AZC}^{b_{AZ}}(r_0, r)$ from (2.11) and then in the substitution of dC in (2.2).

The specific attenuation profile follows from the use of the A-Z relationship (2.5):

$$A_{AZC}(r) = Z_m(r)^{b_{AZ}} [AF(r_0)^{b_{AZ}} - AF(r_m)^{b_{AZ}}] / \{0.46 b_{AZ} [AF(r_0)^{b_{AZ}} SZ(r, r_m) + AF(r_m)^{b_{AZ}} SZ(r_0, r)]\} \quad (2.18)$$

$$Z_{AZC}(r) = Z_m(r) [AF(r_0)^{b_{AZ}} - AF(r_m)^{b_{AZ}}]^{1/b_{AZ}} / \{0.46 a_{AZ} b_{AZ} [AF(r_0)^{b_{AZ}} SZ(r, r_m) + AF(r_m)^{b_{AZ}} SZ(r_0, r)]\}^{1/b_{AZ}} \quad (2.15)$$

$$A_{AZC}(r) = Z_m(r)^{b_{AZ}} [AF(r_0)^{b_{AZ}} - AF(r_m)^{b_{AZ}}] / \{0.46 b_{AZ} [AF(r_0)^{b_{AZ}} SZ(r, r_m) + AF(r_m)^{b_{AZ}} SZ(r_0, r)]\} \quad (2.16)$$

240 In addition to their independence with respect to dC , it is interesting to note that both the attenuation factor profile and the specific attenuation profile provided by the AZC algorithm does not depend on the a_{AZ} parameter. This parameter is however present in the expression of the reflectivity profile.

2.2.3 AZC algorithm (independent of a_{AZ}):

$$Z_{AZ\alpha}(r) = Z_m(r) SZ(r_0, r_m)^{1/b_{AZ}} / \{dC [AF(r_0)^{b_{AZ}} SZ(r, r_m) + AF(r_m)^{b_{AZ}} SZ(r_0, r)]\}^{1/b_{AZ}} \quad (2.17)$$

$$A_{AZ\alpha}(r) = Z_m(r)^{b_{AZ}} [AF(r_0)^{b_{AZ}} - AF(r_m)^{b_{AZ}}] / \{0.46 b_{AZ} [AF(r_0)^{b_{AZ}} SZ(r, r_m) + AF(r_m)^{b_{AZ}} SZ(r_0, r)]\} \quad (2.18)$$

The attenuation constraint (11) is now used to express a_{AZ} as:

$$a_{AZ} = [dC^{b_{AZ}} (AF(r_0)^{b_{AZ}} - AF(r_m)^{b_{AZ}})] / [0.46 b_{AZ} SZ(r_0, r_m)] \quad (2.19)$$

Mis en forme : Police : Non Italique

Mis en forme : Police : +Titres (Times New Roman)

Mis en forme : Police : +Titres (Times New Roman)

Mis en forme : Police : Non Italique

Mis en forme : Police : Non Italique

Mis en forme : Police : +Titres (Times New Roman)

Mis en forme : Police : +Titres (Times New Roman)

which can be introduced in (2.11) to yield:

$$AF_{AZ\alpha}^{b_{AZ}}(r_0, r) = [AF(r_0)^{b_{AZ}} SZ(r, r_m) + AF(r_m)^{b_{AZ}} SZ(r_0, r)] / AF(r_0)^{b_{AZ}} SZ(r_0, r_m) \quad (2.20)$$

Equation 2.20 is actually identical to the $AF_{AZC}^{b_{AZ}}(r_0, r)$ expression (2.16). From (2.20), (2.2) and (2.3), the resulting corrected reflectivity profile can be expressed as:

$$Z_{AZ\alpha}(r) = Z_m(r) SZ(r_0, r_m)^{1/b_{AZ}} / \{dC [AF(r_0)^{b_{AZ}} SZ(r, r_m) + AF(r_m)^{b_{AZ}} SZ(r_0, r)]\}^{1/b_{AZ}} \quad (2.21)$$

One can note that $Z_{AZ\alpha}(r)$ is different from $Z_{AZC}(r)$ and that it depends on dC .

Next, it can be verified by using (2.21), (2.5) and (2.19) (a second time, for the necessary substitution of a_{AZ}) that the $AZ\alpha$ specific attenuation profile is identical to the AZC specific attenuation profile given by (2.18) with:

$$A_{AZ\alpha}(r) = Z_m(r)^{b_{AZ}} [AF(r_0)^{b_{AZ}} - AF(r_m)^{b_{AZ}}] / \{0.46 b_{AZ} [AF(r_0)^{b_{AZ}} SZ(r, r_m) + AF(r_m)^{b_{AZ}} SZ(r_0, r)]\} \quad (2.22)$$

We emphasize that both the attenuation factor and specific attenuation profiles provided by the AZC and $AZ\alpha$ algorithms are identical. Moreover, they do not depend on the a_{AZ} and dC parameters. This is a priori a very interesting property of these algorithms, exploited in particular by Testud et al. (2000) and Ryzhkov et al. (2014). However, the reflectivity profiles provided by the two algorithms are different and, in particular, the reflectivity profile of the $AZ\alpha$ algorithm depends on dC while the reflectivity profile of the AZC algorithm depends on a_{AZ} .

2.2.4 AZ0 algorithm (independent of a_{AZ}):

The attenuation constraint (2.11) can finally be used to express $AF(r_0)^{b_{AZ}}$ as:

$$AF(r_0)^{b_{AZ}} = [0.46 a_{AZ} b_{AZ} SZ(r_0, r_m) + (AF_m(r_m) dC)^{b_{AZ}}] / dC^{b_{AZ}} \quad (2.23)$$

which can be introduced in (2.11) to yield:

$$AF_{AZ0}^{b_{AZ}}(r_0, r) = \{0.46 a_{AZ} b_{AZ} SZ(r, r_m) + AF(r_m)^{b_{AZ}} dC^{b_{AZ}}\} / \{0.46 a_{AZ} b_{AZ} SZ(r_0, r_m) + (AF_m(r_m) dC)^{b_{AZ}}\} \quad (2.24)$$

Mis en forme : Police : Non Italique

Mis en forme : Police : Non Italique

Mis en forme : Police : Non Italique

Mis en forme : Police : Non Italique

Mis en forme : Police : Non Italique

Mis en forme : Police : Non Italique

Mis en forme : Police : Non Italique

Mis en forme : Police : Gras

The resulting corrected reflectivity profile is:

$$Z_{AZ0}(r) = Z_m(r) / \{0.46 a_{AZ} b_{AZ} SZ(r, r_m) + (AF_m(r_m) dC)^{b_{AZ}}\}^{1/b_{AZ}} \quad (2.25)$$

And the specific attenuation profile:

$$A_{AZ0}(r) = a_{AZ} Z_m(r)^{b_{AZ}} / \{0.46 a_{AZ} b_{AZ} SZ(r, r_m) + (AF_m(r_m) dC)^{b_{AZ}}\} \quad (2.26)$$

$$Z_{AZ0}(r) = Z_m(r) / \{0.46 a_{AZ} b_{AZ} SZ(r, r_m) + (AF(r_m) dC)^{b_{AZ}}\}^{1/b_{AZ}} \quad (2.19)$$

$$A_{AZ0}(r) = a_{AZ} Z_m(r)^{b_{AZ}} / \{0.46 a_{AZ} b_{AZ} SZ(r, r_m) + (AF(r_m) dC)^{b_{AZ}}\} \quad (2.20)$$

The AZ0 algorithm has the simplest mathematical expressions among the three algorithms using the PIA constraint. It looks like a “backward algorithm” since the reflectivity and the specific attenuation profiles estimated at the running range r depend only on the measured reflectivities between ranges r_m and r_m , while the AZC and AZAZ α algorithms make use of the entire measured reflectivity profile between r_0 and r_m for the estimations at range r .

The + signs in the denominators of eqs. 2.18, 2.19, 2.21, 2.22, 2.25 and 2.26 are indicators of the inherent stability of the three algorithms using the PIA constraint, unlike the AZhb algorithm.

2.3 Formulation of a simple polarimetric algorithm

In addition to the present study AZ algorithms, we are making a basic use of polarimetry with the derivation of consider a PIA profile, denoted $PIA_{\Phi_{dp}}(r)$, $PIA_{\Phi_{dp}}(r_0, r)$, derived from the profile of the total differential phase shift on propagation, denoted $\Phi_{dp}(r_0, r)$ [°]:

$$\Phi_{dp}(r_0, r) = 2 \int_{r_0}^r K_{dp}(s) ds \quad (2.2721)$$

where K_{dp} is the specific differential phase shift on propagation [° km⁻¹]. Assuming a power-law relationship between the specific attenuation and the specific differential phase shift on propagation, with:

Mis en forme : Police :Non Italique
 Mis en forme : Police :Non Italique
 Mis en forme : Police :Non Italique
 Mis en forme : Police :Non Italique
 Mis en forme : Police :Non Italique

$$A = a_{AZ} K_{AZ}^{b_{AZ}} A = a_{AK} K_{dp}^{b_{AK}} \quad (2.2822)$$

and using Eqs 2.4 and 2.9 yields:

$$PIA_{\Phi dp}(r) = PIA_0 + 2 a_{AK} \int_{r_0}^r K_{dp}^{b_{AK}}(s) ds \quad (2.29)$$

We obtain:

$$PIA_{\Phi dp}(r_0, r) = 2 a_{AK} \int_{r_0}^r K_{dp}^{b_{AK}}(s) ds \quad (2.23)$$

This polarimetry-derived Δ profile can be related/compared to the Δ profiles obtained by integrating the ΔZ specific attenuation profiles given by Eqs 2.14, 2.18 and 2.26 (equivalently, the $PIA_{\Phi dp}(r)$ profile could be derived as a function of range and related to the ΔZ specific attenuation profiles) 16, (2.18, identical to 2.16) and 2.20 between r_0 and r .

2.4 Analysis of the parameters of the considered physical model

Equations 2.11, 2.12 and 2.2923 form a system of equations with seven parameters (or unknowns), namely the coefficients of the ΔZ relationship ($a_{AZ}, b_{AZ}, \Delta_{AZ}, b_{AZ}$), the coefficients of the $A - K_{dp} A - K_{dp}$ relationship ($a_{AK}, b_{AK}, \Delta_{AK}, b_{AK}$), the radar calibration error (dC_dC), the on-site attenuation (PIA_0) and the path-integrated attenuation at range r_m (PIA_m). We focus in this article on the idea of the rain rate profiles will require two additional parameters, e.g. constraining this system of equations with the two parameters (a_{AZ}, b_{AZ})PIAs derived from the Mountain Reference Technique. The question of the $R - A$ transformation is beyond the scope of the present study.

From a physical point of view, the parameters dC_dC , PIA_0 and PIA_m are mutually independent and a priori independent of the coefficients of the $Z - A - K_{dp}$ power-law models:

- We will assume the radar calibration error to be constant for a given precipitation event, with possible variations from one event to the next.
- Regarding on-site attenuation, Frasier et al. (2013) made a synthesis of previous theoretical and empirical studies, and provided an empirical model based on the comparison of the measurements of two X-Band radar systems in the French Southern Alps, one equipped with a radome and the other one being radomeless. From this article, we take into account a dependence of PIA_0 on the measured reflectivity in the vicinity of the radar site, denoted Z_0 . Based on

Mis en forme : Police :Non Italique

Mis en forme : Police :Non Italique

Mis en forme : Police :Non Italique

Mis en forme : Police :Non Italique

Mis en forme : Police :Non Italique

Mis en forme : Français (France)

350 Figure 5 in Frasier et al. (2013), we have fitted a coarse power-law model for X-band radome attenuation on their experimental data, yielding $PIA_0^* = 0.0126 Z_0^{1.6}$ with PIA_0^* in dB and Z_0 in dBZ. Based on their Fig. 6 which shows important variations between the theoretical and empirical results proposed in the literature, we have defined a large range of lower and upper limits for the PIA_0 draws conditioned on Z_0 via the PIA_0^* model (see Table 1). With $n = 5$, the crude model proposed yields upper limits of the PIA_0 sampling range of 4.8, 9.2, 14.6 and 20.8 dB for Z_0 values of 20, 30, 40 and 50 dBZ, respectively. In the following simulations, PIA_0 will be allowed to vary from one target to the next, i.e. in different directions, and from one time step to the next.

355 • The accuracy of the MRT-derived PIA_m was studied in Delrieu et al. (1999) by comparing MRT estimates with direct measurements obtained with a receiving antenna set up in the mountain range. They showed that (i) selecting strong mountain returns (typically greater than 45-50 dBZ) allows to mitigate the impact of precipitation falling over the target (negative bias), (ii) that a refined estimation of the so-called dry-weather baseline is required to account for the possible modification of backscattering properties of the mountain surfaces before and after the event and (iii) that the time variability of the dry-weather returns defines the minimum detectable PIA. These elements were accounted for in the present study by selecting strong mountain targets, studying their dry-weather time variability (see also Delrieu et al. 2020) and subsequently defining the range of variation of the dAF_m multiplicative error (Table 1).

360 -A relationship. The

365 The prefactors and exponents of the so-called $Z - A - K_{ap} - R$ relationships $Z - A - K_{dp}$ power-law models are mutually dependent since they are determined by the shape, density and size distributions of the hydrometeors and their electromagnetic properties, largely driven by their solid versus liquid composition. These coefficients may vary considerably from one precipitation type to another. In addition, even for a given precipitation type, the actual $Z - A - K_{ap} - R$ relationships $Z - A - K_{dp}$ values present an inherent variability with respect to the power-law models, associated with the greater or lesser proximity of the particle size distribution (PSD) moments associated to each particular variable (e.g. the 6th order PSD moment for the reflectivity, the 3.67th order PSD moment for the rainrate). As an ultimate, As a further complexity, when for a given propagation path various types of hydrometeors are successively encountered (e.g. rain, melting precipitation, snow), it would be desirable to apply the appropriate coefficients for the different precipitation types, provided one is able to determine them.

370 As a major simplification in the present work, we will be considering a homogeneous precipitation type (convective rainfall). Because of the mathematical form of the equations at hand and the likely mutual dependence of the exponent exponent and prefactors prefactor of the each power-law models model, we will assume the exponents of the A-Z and the A - K_{ap} A - K_{dp} relationships to be constant for all the considered events while the prefactors will be allowed to vary for each single target and time step. The question of the R-A conversion is left aside in this study.

380 There has been several studies deriving A-Z and A - K_{dp} relationships at X-Band using different approaches including model calculations and also the direct use of observational data (e.g., Bringi and Chandrasakar, 2001; Gorgucci and Chadrasar, 2001).

Mis en forme : Paragraphe de liste, Avec puces + Niveau : 1
+ Alignement : 0,63 cm + Retrait : 1,27 cm

Mis en forme : Police :Non Italique

Mis en forme : Police :Non Italique

Mis en forme : Police :Non Italique

2005, Park et al. 2005, Schneebeli et al. 2012, Matrosov et al. 2014, Yu et al. 2018). Estimations of these coefficients and their ranges of variation were obtained in our study by processing the drop size distribution (DSD) data collected with a PARSIVEL 2 disdrometer located at the IGE site. The dataset includes 337 rainy days during the period April 2017 – March 2020. The raw DSD measurements have a time resolution of 1 min. They are binned into 32 diameter classes with increasing sizes from 0.125 mm up to 6 mm. Various filters have been applied to discard anomalous data and, in particular to detect non-liquid precipitation, thanks to the falling speed spectra. The volumetric concentration spectra have been computed at a 5-min resolution. DSD spectra with 5-min rainrate less than 0.1 mm h^{-1} were discarded from the analysis. A dataset of about 14600 DSD spectra was thus obtained corresponding to all types of precipitation occurring in liquid phase in the Grenoble valley. As for the scattering model, we used the CANTMAT version 1.2 software programme that was developed at Colorado State University by C. Tang and V.N. Bringi. The CANTMAT software uses the T-Matrix formulation to compute radar observables such as horizontal reflectivity, vertical reflectivity, differential reflectivity, co-polar cross-correlation, specific attenuation, specific phase shift, etc. as a function of the DSD, the radar frequency, air temperature, oblateness models and canting models for the raindrops as well as the incidence angle of the electromagnetic waves. The results presented herein were computed for the X-band frequency, a temperature of 10°C , the Beard and Chung (1987) oblateness model, a standard deviation of the canting angle of 10° and an incidence angle of 0° (horizontal scanning, like for the MOUC radar data).

Figure 3 illustrates the fittings of the $A - Z$ relationships that can be obtained from a classical logarithm of base 10 transformation of the two variables. One can note that the scatterplot is well conditioned for deriving a power-law model in the sense that it does not present any particular curvature. The least-square regressions of A over Z and of Z over A as well as the least-rectangle regression are displayed to illustrate the impact of the regression technique on the model coefficients. Note that the least-rectangle fit should be preferred since, for these calculations based on DSD data, the two variables can be considered on an equal footing. The determination coefficient is high and the three regressions performed give subsequently parameter sets close to each other. From the fittings in Fig. 3, we have chosen $b_{AZ} = 0.8$ as a fixed value for this exponent and $a_{AZ} = 1.0 \cdot 10^{-4}$ as the central value for the sampling of the prefactor in the following sensitivity analysis. Although the scatter of the points around the power-law model suggests a possible range of variation of $[-5, 5 \text{ dB}]$ for the DSD-derived values, we have limited this range to $[-3, 3 \text{ dB}]$ in our simulations on the basis of the much bigger resolution volume of the radar and the assumption that the prefactor is constant throughout the reflectivity profile (Table 1).

Figure 4 gives the results obtained for the $A - K_{dp}$ relationship. It can be seen that the scatterplot of the logarithmic of base 10 transformed variables (Fig. 4a) presents a significant curvature. Due to the important weight given to low and medium values in the regressions, the fitted power-law models are clearly unsatisfactory for the highest values, which are of interest in the present study since they correspond to convective precipitation. We have therefore tested two other fitting techniques based on the natural values of the two variables (Fig. 4b). A linear fit with a 0-forced intercept yields $A_h = 0.32 K_{dp}$, which is consistent with linear relationships proposed in the literature in similar climatological contexts, however with a somewhat

420 higher value of the multiplicative coefficient: e.g., 0.245 in Schneebeli et al. (2012) and 0.276 in Yu et al. (2018). However, we note that this linear fit is not satisfactory with a significant underestimation of the A_h values for $K_{dp} > 3 \text{ }^\circ \text{ km}^{-1}$. The fitting of a non-linear power-law model (NLPL) proves to be more satisfactory with $A_h = 0.30 K_{dp}^{1.1}$. Since the exponents estimated with the log-transformed data are close to 0.9, we have decided to perform several simulations with fixed values of b_{AK} in the range [0.9 – 1.2] (see Table 1). Regarding the prefactor a_{AK} , we have considered a central value of 0.3 and a range of variation of [-3, 3dB], that is minimum and maximum values of 0.15 and 0.6, respectively.

425 Additional tests have been performed, including for instance the influence of the air / hydrometeor temperature, the precipitation type (e.g. stratiform versus convective rainfall), the DSD integration time step, etc. Concerning the last factor, we have compared the results obtained for the 2-min and 5-min time steps and we have found no significant influence on the coefficients of the power-law models, while the R^2 values were significantly downgraded for the 2-min time step (not shown here for the sake of conciseness). As for the precipitation type, we carried out a rough classification of the 337 events into stratiform and convective types, by considering an event as convective if a rainrate threshold of 10 mm h^{-1} was exceeded for at least one 5-min time step during the event. As one would expect from the scatterplots in Figs 4 and 5, significant differences appeared between the stratiform and convective $A - K_{dp}$ relationships whereas the $A - Z$ relationships were almost identical. This is an argument for keeping the exponent b_{AZ} constant in our simulation procedure. Regarding the sensitivity on temperature, one possible extension of the present work could be to consider the temperature time series available for each event at the IGE site in the scattering calculations. From a physical point of view, the parameters dC , PIA_0^* and PIA_m^* are mutually independent and *a priori* independent of the coefficients of the $Z - A - K_{dp} - R$ power-law models. It seems reasonable, and this is done in the following simulations, to assume the radar calibration error to be constant for a given precipitation event. This would most likely result in an increase in the variability of the $A - Z$ and $A - K_{dp}$ relationships. As a classical concern, one may however wonder how the average temperature in the radar resolution volume could be estimated (Ryzhkov et al. 2014). We chose herein to rely on the ability of the simulation procedure to deviate from the central values of the parameters and their ranges of variation defined in Table 1 to be large enough.

Mis en forme : Police :Non Italique

Mis en forme : Paragraphe de liste, Avec puces + Niveau : 1
+ Alignement : 0,63 cm + Retrait : 1,27 cm

440

- Regarding on-site attenuation, Frasier et al. (2013) made a synthesis of previous theoretical and empirical studies, and provided an empirical model based on the comparison of the measurements of two X-Band radar systems in the French Southern Alps, one equipped with a radome and the other one being radomeless. From this article, we have devised two sampling strategies for the parameter PIA_0^* . The first sampling strategy is a simple random draw of PIA_0^* between 0 and 10 dB whatever the precipitation conditions at the radar site. The second one takes into account a dependence of PIA_0^* on the measured reflectivity in the vicinity of the radar site, denoted Z_0^* . Based on Figure 5 in Frasier et al. (2013), we have fitted a coarse power-law model for X-band radome attenuation on their experimental data, yielding $PIA_0^* = 0.0126 Z_0^{*0.6}$ with PIA_0^* in dB and Z_0^* in dBZ. Based on their Fig. 6 which shows important variations between the theoretical and empirical results proposed in the literature, we have defined a large range of

450 lower and upper limits for the PIA_g draws conditioned on Z_g via PIA_g^* (see Table 1). For the two sampling
 strategies, PIA_g will be allowed to vary from one target to the next, i.e. in different directions, and from one time step
 to the next. The accuracy of the MRT-derived PIA_m was studied by Delrieu et al. (1999) by comparing MRT
 455 estimates with direct measurements obtained with a receiving antenna set up in the mountain range. They showed
 that (i) selecting strong mountain returns (typically greater than 45-50 dBZ) allows to mitigate the impact of
 precipitation falling over the target (negative bias), (ii) that a refined estimation of the so-called dry-weather baseline
 is required to account for the possible modification of backscattering properties of the mountain surfaces before and
 after the event and (iii) that the time-variability of the dry-weather returns defines the minimum detectable PIA. These
 elements were accounted for in the present study by selecting strong mountain targets, studying their dry-weather
 460 time-variability (see also Delrieu et al. 2020) and subsequently defining the range of variation of the dAF_m
 multiplicative error (Table 1).

3. Sensitivity analysis

3.1. Principle

465 The parameter structure analyzed in sub-section 2.4 led us to organize the optimization-sensitivity analysis procedure in a
 nested way:

For a series of convective all the considered rain events, we assume the exponents of the A-Z and $A \rightarrow K_{ZF} A - K_{dp}$ relationships
 470 to be constant;

For each event, we assume the radar calibration error to be constant. A simulation is performed for each combination of the
 b_{AZ} , b_{AK} , b_{AZ} , b_{AK} and $dGdC$ values listed in Table 1, i.e. $1 \times 6 \times 13 = 78$ simulations.

The
 475 For each mountain target and each time step, the simulation "core" is implemented as follows for each mountain target and
 each time step:

- The $Z_m(r)$ and $\Phi_{dp}(r)$ profiles between the radar and the mountain target are pre-processed. For each of
 the successive radials composing the target, this includes determination of gates affected by clutter in the region of
 the mountain target and along the propagation path. This is done by considering both dry-weather mean values
 exceeding various thresholds (25 dBZ for significant clutter, 45 dBZ for a gate belonging to the mountain target) and
 480 by using the profile of the copolar correlation coefficient (ρ_{hv}) (Delrieu et al. 2020). The median $Z_m(r)$ and
 $\Phi_{dp}(r)$ profiles over the series of radials are then computed. The MRT PIA_m is evaluated as the
 difference of the Z_m mean values between the dry-weather baseline and the current time step, the mean being taken

Mis en forme : Police : Non Italique

Mis en forme : Retrait : Première ligne : 0 cm

over all the gates composing the target. The r_0 value is estimated as the range of the first gate for which four successive values (corresponding to a range extent of 960 m) exceeds a $\rho_{\text{prec}} \rho_{\text{hv}}$ value of 0.95. This last value is set as a threshold between precipitation and clutter / no precipitation (from the statistics presented in Khanal et al. 2019). The Z_0 value is computed as the product of $1/dC$ (correction for the radar calibration error) and the mean reflectivity of the selected four successive gates if they are located within the first 2 km range; otherwise the Z_0 value is set to 0. The reader is referred to Khanal et al. (2022) for the most recent description of the fairly sophisticated procedure used for the $\Phi_{\text{dp}}(r)$ regularization based on the total differential phase shift profiles $\Psi_{\text{dp}}(r)$ for all the radials associated with a given target. Note that a target is selected at a given time step for the following steps of the simulation if $PIA_m > 1$ dB and if a good quality index of the $\Phi_{\text{dp}}(r)$ regularization is obtained (Khanal et al. 2022).

- The Latin Hypercubes Sampling technique (<https://www.rdocumentation.org/packages/pse/versions/0.4.7/topics/LHS>) is then used to generate N parameter sets (with $N = 2000 = 1000$ in the following) filling uniformly the parameter space composed of four parameters: the prefactors a_{AZ} and a_{AK} , the on-site attenuation factor $AF(r_0)$ and the multiplicative error dAF_m (eq. 2.8) on the MRT attenuation factor. The central values and intervals of variation of these four parameters are listed in Table 1. It is noteworthy that the random draws are made on the dB-transformed ranges of parameters so that there are as many values below and above the central value, e.g. as many values between 0.15 and 0.3 on the one hand and between 0.3 and 0.6 on the other hand for the a_{AK} parameter.
- After discarding unphysical parameter sets (e.g. those leading to $PIA_0 > PIA_m$), the five algorithms are implemented for all the remaining sets. A cost function (CF) is evaluated in order to measure the convergence / proximity of the five simulated profiles for each parameter set. The several formulations of the cost function were tested and we propose the following CF one hereinafter, which was found to be appropriate:

$$CF = \text{Mean}(NSE(Z_{AZhb}(r), Z_{AZC}(r)),$$

$$\text{NSE}(Z_{AZC}(r), Z_{AZ\alpha}(r)),$$

$$\text{NSE}(Z_{AZC}(r), Z_{AZ0}(r)),$$

$$\text{NSE}(Z_{AZ\alpha}(r), Z_{AZ0}(r)),$$

$$\text{NSE}(PIA_{AZC}(r), PIA_{\Phi dp}(r)),$$

$$\text{NSE}(PIA_{AZ0}(r), PIA_{\Phi dp}(r)))$$

$$CF = \text{Mean}(R^2(PIA_{AZhb}(r_0, r), PIA_{AZC}(r_0, r)),$$

$$R^2(PIA_{AZhb}(r_0, r), PIA_{AZ0}(r_0, r)),$$

$$R^2(PIA_{AZhb}(r_0, r), PIA_{\Phi dp}(r_0, r)),$$

$$R^2(PIA_{AZC}(r_0, r), PIA_{AZ0}(r_0, r)),$$

Mis en forme : Police :Non Italique

Mis en forme : Police :Non Italique

Mis en forme : Police :Non Italique

$$R^2(\text{PIA}_{AZC}(r_0, r), \text{PIA}_{\Phi dp}(r_0, r)),$$

$$R^2(\text{PIA}_{AZ0}(r_0, r), \text{PIA}_{\Phi dp}(r_0, r))$$

(3.1)

520

where Mean stands for “the mean value of” and NSE is the Nash-Sutcliffe efficiency (Nash and Sutcliffe, 1970) determination coefficient between the two profiles indicated between brackets. The NSE criterion, or efficiency, is quite popular in hydrological sciences. It is employed in the context of parameter optimization since it has the definite advantage of being sensitive to both the average values and the correlation of the compared data series. Note that NSE = 1 denotes perfect agreement between the two series. The first four terms of the CF allow measuring the convergence of the four AZ reflectivityThe profiles that considered in this expression of the cost function are different from each other (unlike the PIA profiles between ranges r_0 and r . Since the specific attenuation profiles of the AZC are identical for the AZC and AZ α formulations (eqs. 2.16 and AZ α algorithms, see section 2.2). 18), only the PIA profile of the first is considered in eq. 3.1. Due to the inherent instability of the AZhb algorithm, we consider the first NSE term three R² terms in the computation of the CF value only if $\text{PIA}_m - \text{PIA}_0 < 10$ dB. Indeed, this 10 dB value proved to be about the maximum valuePIA this algorithm is able to deal with, even with an almost perfect parameterization (Delrieu et al. 1999b). The last twothree terms of the CF are measuring the proximity of the polarimetric algorithm with the AZC and AZ0 algorithms in terms of the PIA profiles. Averaging NSE values computed for reflectivity and PIA profiles is acceptable since the ranges of variation of these two variables are of the same order of magnitude (note that this would not be the case for reflectivity and specific attenuation profiles). three PIA-constrained algorithms. In the following, we have selected $\text{CF}_{th} = 0.8$ as the “satisfaction threshold”, i.e. the CF value to be exceeded to consider a given parameter set as “optimal”.

525

530

535

540

545

The acronym OPS will be used for “optimal parameter set” and NOPS for “hereinafter. The number of optimal parameter sets” will be used hereinafter. The NOPS (NOPS) can be computed for a given target and time step and summed up for all the targets and time steps of an event and for a series of events to yield a measure of the overall quality of a given simulation involvingfor given fixed parameters ($b_{AZ}, b_{AK}, dCb_{AZ}, b_{AK}, dC$) and randomly drawn parameters ($a_{AZ}, a_{AK}, AF(r_0), dAF_{th}, dAF_m$) for each single target / time step using the LHS technique. We recognise that the choice of the cost function (eq. 3.1) and the “satisfaction threshold” CF_{th} are essentially subjective. They relyThis choice relies on the experience gained duringin the implementingimplementation of the simulation framework. TwoThree elements can be mentioned on this subject: (i) accounting for the AZhb algorithm in the CF for low to moderate PIAs less than 10 dB proved to be a good option owing to the strong sensitivity of this algorithm on the calibration error; (ii) adding the polarimetric algorithm and the subsequent last two NSEs corresponding R² terms in the CF allowed to dramatically reduce the mathematical ambiguity (i.e. the fact that several combination of parameters, including non-physical values, may lead to the convergence of

Mis en forme : Police :Non Italique

Mis en forme : Police :Non Italique

Mis en forme : Police :Non Italique

Mis en forme : Police :Non Italique

Mis en forme : Police :Non Italique

Mis en forme : Police :Non Italique

Mis en forme : Police :Non Italique

Mis en forme : Police :Non Italique

Mis en forme : Police :Non Italique

the solutions of the different algorithms) of the physical model at hand. This ambiguity is indeed quite large for the AZ algorithms considered alone, in particular, (iii) several satisfaction thresholds were tested with regard to low sensitivity on the dC , α_{AZ} and $AF(r_0)$ results in terms of the quantiles of the statistical distributions of the estimated parameters.

3.2. Results

3.2.1 Illustration for a given target and time step

Figure 35 gives an example of result of the core procedure for target 13 (T13) on 21 July 2017 16:05 UTC. For this case with a MRT PIA of 25.9 dB at a range of about 20 km, we get $\Phi_{AP}(r_0, \Phi_{dp}(r_0, r_{m1}, r_m)) = 71.5^\circ$ and $Z_{AZ0} = 9.5$ dBZ. The optimal set of fixed parameters for the considered event is $dC^* = 0.45$ dB, $b_{AZ} = 0.788$ and $b_{AK}^* = 1.1$ (see next sub-sections). Since for the best OPS, all the reflectivity profiles overlap perfectly, the results presented in Fig.3 correspond actually to a less near-optimal set so that one can see some differences between the solutions of the different algorithms. The set of optimal "LHS-sampled" parameters for this specific target / time step is $PIA_0^* = 0.46$ dB, $\alpha_{AZ}^* = 1.01 \cdot 10^{-4}$, $\alpha_{AK}^* = 0.34$ and $dAF_m^* = 0.99$. The CF value is 0.925, while the CF value one obtained with the best OPS is 0.981. Note that 55 parameter sets overpassed the CF threshold value of 0.8 for this example, i.e. $\#OPS \geq 0.8 = 55$ for this target and time steps. For this good (though not the best) OPS, the reflectivity profiles (Fig. 3a5a) call for the following comments. We have here a clear example of the inherent instability of the AZhb algorithm, which "blows up" at a range of about 7 km for this parameterization. One should remember that this algorithm is not accounted for in the CF computation for such high PIAs, as explained in sub-section when commenting eq. 3.1. The three other AZ algorithms give rather similar results. As a general behaviour (and in particular whatever the value of the on-site attenuation), we note that the optimal parameterizations lead to the convergence of the AZC and AZ0 algorithms near the radar and to the convergence of the AZ α and AZ0 algorithms on at the other end of the profile. Fig 3b5b gives the solutions obtained in terms of specific attenuation profiles. The AZhb profile is not drawn in this figure. As shown in sub-section 2.2, the AZ α and AZC solutions are identical (represented in red) and slightly different at long range from the AZ0 solution. The comparison of the corrected and uncorrected profiles clearly shows in this example the dramatic impact of attenuation as regard to both the underestimation of the first precipitation cell and the non-detection of the second one. Fig. 3e5c displays the raw and processed Φ_{AP} - Φ_{dp} profiles. For such a strong attenuation case, one can see that the raw profile has little noise and no significant "bumps" that could sign a differential phase shift on backscattering (δ_{np} - δ_{nv}) contamination (Trömel et al., 2013). Finally, Fig. 3d5d allows comparison of the PIA profiles derived from the AZC-AZ α algorithms (identical solutions), the AZ0 algorithm and from the Φ_{AP} - Φ_{dp} profile. Although there are some differences, the overall consistency between the three profiles is good.

3.2.2 Time series of optimal parameter values

Mis en forme : Police :Non Italique

Mis en forme : Police :Non Italique

Mis en forme : Police :Non Italique

Mis en forme : Police :Non Italique

Mis en forme : Police :Non Italique

Mis en forme : Police :Non Italique

Mis en forme : Police :Non Italique

Mis en forme : Police :Non Italique

Mis en forme : Police :Non Italique

Mis en forme : Police :Non Italique

Mis en forme : Police :Non Italique

Mis en forme : Police :Non Italique

Mis en forme : Police :Non Italique

Mis en forme : Police :Non Italique

Mis en forme : Police :Non Italique

Mis en forme : Police :Non Italique

Mis en forme : Police :Non Italique

Mis en forme : Police :Non Italique

Mis en forme : Police :Non Italique

Mis en forme : Police :Non Italique

Mis en forme : Police :Non Italique

Mis en forme : Police :Non Italique

Figure 46 presents the time series of quantiles of the distributions of the input variables and the estimated optimal parameters obtained for the best simulation of the 21 July 2017 convective event. The second sampling strategy making use of $Z_{\text{g}}Z_0$ (see Table 1) is considered for PIA_g in this example. We will come back in sub-section 3.2.5 on the relationship between PIA_g (Fig. 4e6c) and $Z_{\text{g}}Z_0$ (Fig. 4a6a). The time series of the medians of PIA_m and $\Phi_{\text{dp}}(r_m)$ (Fig. 6b) give an indication on the evolution of the storm intensity which was greater intense between 15:30 and 17:00 UTC with medians of about 20 dB and 60°, respectively. The interquartile ranges of these two variables are quite large, as a result of both the variation of the radar-target distances (from 15 up to 40 km) and the precipitation variability as a function of the azimuth, illustrated in Figs 1 and 2. The time evolution of the storm intensity is more marked also visible on the NOPS time series (Fig. 4f6f) with multiplicative factors in the range of 5 to 10 between the period 16:00-17:00 and the period 17:00-18:00 UTC. Although for a given target, there is an increasing trend of NOPS when PIA_m increases (not shown for the sake of conciseness), this is also related to the higher number of targets “reached” (i.e. targets with PIA_m values greater than 1 dB) between 16:00 and 17:00 UTC. We draw the attention The time series of the prefactors a_{AK} (Fig. reader to the low NOPS values6d) and to the singular a_{AZ} (Fig. 6e) have a similar behaviour with rather stable median values, that are close to the central values obtained for the optimal parameters (Figs 4cde) at time step 17:00 UTC compared with the rest of the time series. This is related to the strong on-site attenuation already evidenced on Fig. 2 (bottom graphs), which will be discussed in more detail in sampling intervals derived from the analysis of the DSD data (sub-section 3.2.5).

Some explanations are required at this stage regarding4, Table 1). This is reassuring as to the choice made in the present simulation exercise relevance for the values and ranges of variation of the prefactors and exponents of the $A-Z$ and $A-K_{\text{dp}}$ relationships. Estimations were obtained from the radar data processing of the drop size distribution (DSD) data collected with a PARSIVEL 2 disdrometer located at the IGE site. these DSD-derived relationships deduced from in-situ microphysical The dataset includes 237 rainy days during the period April 2017 – March 2020. The raw DSD measurements and have a time resolution of 1 min. They are binned into 32 diameter classes with increasing sizes from 0.125 mm up to 6 mm. Various filters (Hachani et al., 2017) were applied to discard anomalous data and, in particular to detect non-liquid precipitation, thanks to the falling speed spectra. The volumetric concentration spectra were then computed at a 5-min resolution. DSD spectra with 5-min rain rate less than 0.1 mm h^{-1} were discarded from the analysis. A dataset of about 14600 DSD spectra was thus obtained corresponding to all types of precipitation occurring in liquid phase in the Grenoble valley. As for the scattering model, we used the CANTMAT version 1.2 software programme that was developed at Colorado State University by C. Tang and V.N. Bringi. The CANTMAT software uses the T-Matrix formulation to compute radar observables such as horizontal reflectivity, vertical reflectivity, differential reflectivity, co-polar cross correlation, specific attenuation, specific phase shift, etc, as a function of the DSD, the radar frequency, air temperature, oblateness models and canting models for the raindrops as well as the incidence angle of the electromagnetic waves. The results presented herein were computed for the X-band frequency, a

Mis en forme : Police :Non Italique

Mis en forme : Police :Non Italique

Mis en forme : Police :Non Italique

615 temperature of 10°C, the Beard and Chung (1986) oblateness model, a standard deviation of the canting angle of 10° and an incidence angle of 0° (horizontal scanning, like for the MOUC radar data).

620 Figure 5 illustrates the fittings of the $A-Z$ relationship obtained from a classical logarithm of base 10 transformation of the two variables. One can note that the scatterplot is well conditioned for deriving a power-law model in the sense that it does not present any particular curvature. The models provide good fits for the highest values, which correspond to convective rainfall. The determination coefficient is high and the three regressions performed give subsequently parameter sets close to each other. Our choice is to select the least rectangle fit since for these calculations based on DSD data, the two variables can be considered in an equal footing. From this analysis, we have chosen (Table 1) $b_{AZ} = -0.79$ as a fixed value for this exponent and $a_{AZ} = 1.0 \cdot 10^{-4}$ as the central value for the LHS sampling of the prefactor. Although the scatter of the points around the power-law model suggests a possible range of variation of [-5, 5 dB] for the DSD-derived values, we have limited this range to [-3, 3 dB] in our simulations on the basis of the much bigger resolution volume of the radar and the assumption that the prefactor is constant throughout the reflectivity profile.

630 Figure 6 gives the results obtained for the $A-K_{AP}$ relationship. It can be seen that the scatterplot of the logarithmic of base 10 transformed variables (Fig. 6a) presents a significant curvature. Due to the important weight given to low and medium values, the fitted power-law models are clearly unsatisfactory for the highest values, which are of interest in the present study. We have therefore tested two other fitting techniques based on the natural values of the two variables (Fig. 6b). A linear fit with a 0 forced intercept yields $A_n = 0.32 K_{AP}$, which is consistent with linear relationships proposed in the literature (Schneebeli et al. 2013). However, once again, we note that this linear fit is not good for the highest values. The fitting of a non-linear power-law model (NLPL) proves to be more satisfactory with $A_n = 0.30 K_{AP}^{1.1}$. Since the exponents estimated with the log-transformed data are close to 0.9, we have decided to perform several simulations with fixed values of b_{AZ} in the range [0.9—1.2] (see Table 1). Regarding the prefactor a_{AZ} , we have considered a central value of 0.3 and a range of variation of [-3, 3dB], that is minimum and maximum values of 0.15 and 0.6, respectively.

640 Additional sensitivity tests can be performed on such DSD-derived relationships, including for instance the influence of the air/hydrometeor temperature, the precipitation type (e.g. stratiform versus convective rainfall), the DSD integration time step, etc. Concerning the last factor, we compared the results obtained for the 2-min and 5-min time steps and we found no significant influence on the coefficients of the power-law models, while the R^2 values were significantly downgraded for the 2-min time step (not shown here for the sake of conciseness). As for the precipitation type, we carried out a rough classification of the 337 events into stratiform and convective types, by considering an event as convective if a rainrate threshold of 10 mm h^{-1} was exceeded for at least one 5-min time step during the event. As one would expect from the scatterplots in Figs 5 and 6, significant differences appeared between the stratiform and convective $A-K_{AP}$ relationships whereas the $A-Z$ relationships were almost

Mis en forme : Police : Non Italique

identical. This is an argument for keeping the exponent b_{AZ} constant in the simulation procedure. Regarding the sensitivity on temperature, one possible extension of the present work could be to consider the temperature time series available for each event at the ICE site in the scattering calculations. This would most likely result in an increase of the variability of the A-Z and A - K_{dp} relationships. As a classical concern, one may however wonder how the average temperature in the radar resolution volume could be estimated (Rhyzhkov et al. 2014). We chose herein to rely on the ability of the simulation procedure to deviate from the central values of the parameters and their ranges of variation to be large enough.

The time series of the prefactors a_{AZ} (Fig. 4d) and a_{AZ} (Fig. 4e) exhibit similar behaviour with (i) median values close to the central values for the most intense part of the event between 16:00 and 16:50 UTC as well as between 17:15 and 17:45, (ii) significant deviations for the most on-site attenuation prone time steps (lower medians between 15:30 and 16:00 UTC and higher median at 17:00 UTC) and (iii) more erratic behaviour from one step to the next after 17:45 UTC at the end of the storm. The first point in the previous list is reassuring in terms of the possibility of using DSD-derived power-law models, and particularly the DSD-derived A-R relationship, for radar QPE. The second point is difficult to explain from a physical point of view. Coupled with the observation that the interquartile ranges are quite large, especially those of the $a_{AZ}a_{AZ}$ parameter, we believe. This is an indication that the mathematical ambiguity (Haddad et al., 1995) of the system of equations at hand remains important. It is noteworthy to mention that the mathematical ambiguity of the AZ algorithms alone is much larger (e.g. with larger interquartile ranges for the $a_{AZ}a_{AZ}$ parameter). Introducing the constraints related to the polarimetric algorithm and the associated constraints on the coefficients of the A - K_{dp} relationship allowed to reduce it dramatically. (not shown for the sake of conciseness).

Figure 7 presents additional results for the 21 July 2017 event with the evolution of the medians at the event time scale of estimated PIA_0 (Fig. 7a), prefactor of the A-Z relationship (Fig. 7b) and prefactor of the A - K_{dp} relationship (Fig. 7c) as a function of the calibration error, for two values of the b_{AK} exponent (1.0 and 1.1). For convenience, the variable $dZ = -dC$ is used in Fig. 7 to represent the dBZ value to be added to the measured reflectivities for correcting the calibration error. We note that the calibration error has a significant impact on the median and interquartile range of PIA_0 , with, logically, stronger on-site attenuations for negative dZ values. The prefactors, expressed in dB relative to the central values in Fig. 7, show a slighter and opposite trend to increase as dZ increases. We also note the marked influence of the b_{AK} exponent on the two prefactors with an offset of about 0.9 and 0.65 dB on the medians of a_{AZ} and a_{AK} , respectively, for $dZ = 0$.

3.2.3 Estimating the radar calibration error

In order to increase the robustness of the results, the simulation procedure was performed for three convective events that occurred successively during summer 2017. Table 2 presents some characteristic features of these events. For all of them the

Mis en forme : Police :Non Italique

melting layer (ML) altitude, determined with the 25°-elevation XPORT radar data by using the procedure developed in Khanal et al. 2019, was situated well above the altitude of the Moucherotte Mount radar, hence, there is no ML contamination of the considered radar data. The first two events were rather intense and similar in terms of total rain amount and maximum rainrate at the IGE site, as well as in terms of the PIA_m statistics based on the 22 mountain targets. The third one was a bit less intense. To our knowledge, there was no occurrence of hail reported in the area of interest for these three events.

We propose to consider the total NOPS obtained for a given simulation and for a given event as a quality criterion to judge the relevance of a set of fixed parameters (dC, b_{AZ}, b_{AK}). Figure 78 shows the NOPS evolution of NOPS for the three events separately and all together as a function of the fixed values of dC listed in Table 1. The optimal values of dC , the other fixed parameters are considered in these results with b_{AZ} being $b_{AZ} = 0.788$ and $b_{AK}^* = b_{AK} = 1.1$; in this figure We note that the various curves are rather flat near their optimum values, e.g. with a ratio between the maximum NOPS value and the nearest value, 0.4 dB apart, of 1.02 when the data of the three events are grouped. The overall sensitivity of the dC parameter calibration error is clear however in the considered [-2, 2 dB] range, e.g. with a ratio of the maximum to the minimum NOPS values of 2.0414 for the all-events curve. Although the global results tend to indicate a very slight underestimation an almost perfect calibration of the measured reflectivities; (optimal dZ value - dZ^* in the following - of 0.25 dBZ), one can note that the optimal dC dZ^* values vary from one event to the next. The with -0.5 dBZ for the 21 July 2017 event is different from, 1.0 dBZ for the other two 8 August 2018 event and the results suggest on the contrary a slight overestimation of 0.5 dBZ for the reflectivities in that case 31 August 2017 event. We find it difficult to know whether such variations in the electronic calibration of the radar from one event to the next could be physically realistic. In any case, an in-depth analysis of By eliminating the data from time series showed steps with significant on-site attenuation, we checked that on-site attenuation could not be held responsible for this result, these dZ^* variations.

3.2.4 Linearity of the $A - K_{dp}A - K_{dp}$ relationship

Similarly, Fig. 9 shows the simulation results evolution of the NOPS criterion computed for the series of b_{AK} values listed in three events all together as a function of the dZ and b_{AK} (Table 1) values. We note a slight superiority of the simulations with $b_{AK} = 1.1 b_{AK}$ in the range [1.05-1.15] compared to the one with $b_{AK} b_{AK} = 1.0$ in terms of the NOPS maximum value of the NOPS computed over the three events all together. This observation is also valid for each of the three events separately (not shown), for clarity in plotting). The simulation with $b_{AK} b_{AK} = 0.9$ is clearly below the other two ones. For $b_{AK} b_{AK} = 1.1$ and for the optimal dZ value of each event, the log-transformed distribution of $a_{AK} a_{AK}$ computed over the three events is nearly symmetrical with an average value of 0.27528 and an interquartile range of nearly about [-1, 1 dB]. Hence, we obtain in this study quite a remarkable agreement between the radar and DSD-derived $A - K_{dp}A - K_{dp}$ relationships for convective precipitation, with $AA = 0.275 K_{dp}^{1.1} K_{dp}^{1.1}$ and $AA = 0.30 K_{dp}^{1.1} K_{dp}^{1.1}$, respectively. Similarly,

Mis en forme : Police : Non Italique

the optimal A - Z relationship derived from the simulation exercise is very close to the one obtained by the DSD measurements

715 (Fig. 3) with $A = 1.07 \cdot 10^{-4} Z^{0.80}$.

3.2.5 Radome attenuation

720 Coming back to Figure 46, we remind that the ~~second~~ sampling strategy making use of $Z_{\text{g}}Z_0$ was considered for the random drawing of $PIA_{\text{g}}PIA_0$ values in this simulation. With $n = 3.0$, the ~~crude model proposed in Table 1 yields upper limits of the PIA_{g} sampling range of 3.0, 5.8, 9.2 and 13.1 dB for Z_{g} simulation values of 20, 30, 40 and 50 dBZ, respectively.~~ One has to remark that such close-range reflectivity measurements are actually affected by radome attenuation. This may explain why estimated $PIA_{\text{g}}PIA_0$ values are ~~of the same order of magnitude~~ higher for time step 17:00 UTC than for time steps between 15:30 and 15:55 while $Z_{\text{g}}Z_0$ values are about 10 dBZ higher in ~~this second~~ the latter period. ~~Thus the~~ The relevance of the $Z_{\text{g}}Z_0$ variable for detection and quantification of on-site attenuation ~~may remain~~ remains limited for a radar equipped with a radome. Nevertheless,

730 Figure 7 shows the comparison of the two PIA_{g} sampling strategies making use or not of Z_{g} (blue and red continuous curves), by reference to the *NOPS* variable computed for the three convective events. This figure clearly evidences a superiority of the strategy taking into account, even in a crude manner, the precipitation conditions at the radar site.

735 Figure 910 gives two examples of the core procedure implementation in the case of severe on-site attenuation that occurred on 21 July 2017 at 17:00 UTC (Fig. 2 bottom graphs). The constraint on the PIA_{g} maximum value for the PIA_0 sampling model as a function of Z_0 was relaxed by considering $n = 10$ in the model of Table 1, that is upper limits of PIA_{g} sampling range of 15.2 and 29.1 dB for Z_{g} these calculations with a maximum PIA_0 values of limit set to 30 and 40 dBZ, respectively dB whatever Z_0 . The mountain returns from Target 04 (T04) allow to quantify both on-site attenuation and along-path attenuation due to precipitation falling over the city of Grenoble (NE sector) at that time (left-hand side example). At this range of about 40 km, we get $PIA_{\text{m}}PIA_0 = 47.9$ dBdB and $\Phi_{\text{dp}}(r_0, r_m) = 129.9^\circ$. The mountain returns from Target 19 (T19) located in the South-East sector (right-hand side) seem to be essentially affected by the precipitation conditions at the radar site. At this range of about 27 km, we get $PIA_{\text{m}}PIA_0 = 11.9$ dBdB and $\Phi_{\text{dp}}(r_0, r_m) = 12.2^\circ$. This yields $PIA_{\text{m}}PIA_0 / \Phi_{\text{dp}}(r_0, r_m)$ ratios of 0.37 and 0.97 dB degree⁻¹ for the two targets, respectively. These values are clearly (especially the second one) well above the range of expected values for the slope of a supposedly linear $A - K_{\text{dp}}A - K_{\text{dp}}$ relationship (Schneebeil et al. 2013), which in In addition to the generalized decrease of the mountain returns, visible in Fig. 2, this is an indication of a significant large on-site attenuation effect. The ΔC -corrected $Z_{\text{g}}Z_0$ values computed in the directions of the two targets are significantly different with 38.9 and 28.6 dBZ, respectively. One can observe the very good convergence of all the AZ algorithms in both cases. In particular for T19, all the AZ reflectivity profiles, including the AZhb

Mis en forme : Police : Non Italique

Mis en forme : Police : Non Italique

Mis en forme : Police : Non Italique

Mis en forme : Police : Non Italique

one, are perfectly matched. The agreement is also very good between the PIA profiles of the AZ algorithms and the one of the polarimetric algorithm, except for a very slight stall of $PIA_{\text{AZ}}(\pm PIA_{\text{AZ}})$ at a range of about 30 km for T04, likely due to disturbances associated with side-lobe effects (visible on the ρ_{HV} PPI on top of Fig. 910).

For the two OPS considered in Fig. 910, one gets PIA_{AZ} values of 10.1 and 10.8 dB. By considering the PIA_{AZ} statistical distribution calculated over the optimal parameter sets of all the targets for the considered time step, one obtains a symmetrical distribution with a slightly higher mean value of 12.6 dB and a rather large interquartile range of 4.5 dB. The mean value increases somehow (13.5 dB) and the interquartile range decreases to 3.2 dB if the PIA_{AZ} distribution is computed for targets 9-22 only, i.e. for targets with reduced along-path attenuation. It is worth noting that such statistics are not improved (e.g., interquartile range reduced) if one considers a more stringent satisfaction criterion (e.g. $CF_{\text{th}} = 0.9$ instead of $CF_{\text{th}} = 0.8$).

4. Discussion and future work

In this paper, we have started to implement a global approach simulation framework to study the interactions between X-band microwaves and hydrometeors in a mountainous context. Emphasis was placed on the attenuation problem, which is known to be severe for the frequency under consideration and essentially uncorrectable unless estimates of total attenuation are available at a distance from the radar. The RadAlp experiment allows us to obtain direct PIA estimates from the Mountain Reference Technique in some specific directions and indirect estimates from the processing of the profiles of total differential phase shift available for each radial. Although the polarimetric technique is a priori much more convenient to apply and has interesting characteristics (independence on radar calibration, on-site attenuation and partial beam blockages), it suffers from several limitations, including (i) the fact that the Ψ_{AZ} profile is noisy for light precipitation, (ii) possible contaminations by the differential phase shift on propagation backscatter δ_{HV} (ii) possible impact of non-uniform beam filling and (iii) the need to specify the relationship between the specific attenuation and the specific differential phase shift which depends on hydrometeor types, temperature, and so on. In a similar way to the satellite configuration (e.g. the possibility to use the Surface Reference Technique in addition to the dual-frequency measurements at Ka and Ku Bands for processing the radar data of the GPM core platform ; Meneghini et al. 2020), we have proposed to take advantage of all the MRT and polarimetric measurements available to perform a generalized sensitivity analysis of the physical model of interest. In the simple case of convective precipitation, (i.e. without "contamination" of radar data by snow or melting precipitation), we have obtained interesting results regarding the estimation of radar calibration, the error, radome attenuation and the coefficients of the $A-Z$ and $A-K_{\text{AZ}}$ relationships. We note that for the estimated optimal radar calibration error, the $A-Z$ and $A-K_{\text{AZ}}$ relationships derived from radar data are consistent with those derived from concomitant drop size distribution measurements at ground level, in particular with a slightly non-linear $A-K_{\text{AZ}}$ relationship ($AA = 0.275 K_{\text{AZ}}^{1.1} K_{\text{AZ}}^{1.1}$). This is

Mis en forme : Police :Non Italique

Mis en forme : Police :Non Italique

Mis en forme : Police :Non Italique

Mis en forme : Police :Non Italique

Mis en forme : Police :Non Italique

Mis en forme : Police :Non Italique

Mis en forme : Police :Non Italique

780 reassuring regarding the relevance of [the use of](#) microphysical data and scattering models for the ~~radar QPE~~-parameterization
of [radar data processing](#). We have deliberately left aside the question of the specific attenuation - rainrate conversion in this
article. An interesting validation exercise to be performed consists in using the DSD-derived ~~A - RA - R~~ relationship for the
conversion of the estimated specific attenuation profiles; ~~then these~~. [The resulting](#) radar rainrate estimates will be compared
with the rain gauge measurements available. Another outcome of the study is the quantification of X-Band radome attenuation.
785 Values as high as 15 dB were estimated, leading to the recommendation of avoiding the use of radomes for remote sensing of
precipitation at such frequency. As an alternative, it would be desirable to develop specific sensors to detect / quantify the
presence of water on the radome wall. ~~The study showed that the measured reflectivity at the radar site is not a good predictor~~
for radome attenuation. (Mancini et al. 2017). As a next step, we plan to extend the procedure to stratiform events with MOUC
radar measurements made at times within or above the melting layer. The multi-angle, multi-frequency, polarimetric
790 measurements of the valley-based radars will be critical in this respect for the characterization of the ML from below (Khanal
et al. ~~2019, 2022~~2019, 2022). [the parameterization of Z-A-K_{dp}-R relationships for different hydrometeor types](#) and the
mitigation of the mathematical ambiguity of the physical model of interest.

795

[Appendix A: Formulation of the attenuation-reflectivity algorithms](#)

800 [A.1 AZhb algorithm \(independent of PIA_m\)](#)

[This formulation is based on \(2.11\) only. In other words, it does not make use of PIA_m. By combining \(2.11\), \(2.2\) and \(2.3\),
one obtains a corrected reflectivity profile through the following equation:](#)

$$805 \quad Z_{AZhb}(r) = Z_m(r) / [(AF(r_0) dC)^{b_{AZ}} - 0.46 a_{AZ} b_{AZ} SZ(r_0, r)]^{1/b_{AZ}} \quad (A.1)$$

[The specific attenuation profile follows from the use of the A-Z power-law model \(2.5\):](#)

$$810 \quad A_{AZhb}(r) = a_{AZ} Z_m^{b_{AZ}}(r) / [(AF(r_0) dC)^{b_{AZ}} - 0.46 a_{AZ} b_{AZ} SZ(r_0, r)] \quad (A.2)$$

[A.2 AZC algorithm \(independent of dC\)](#)

Mis en forme : Police :Non Italique

The attenuation constraint (2.12) is used to express dC as:

$$dC = [0.46 a_{AZ} b_{AZ} SZ(r_0, r_m) / (AF(r_0)^{b_{AZ}} - AF(r_m)^{b_{AZ}})]^{1/b_{AZ}} \quad (A.3)$$

which is introduced in (2.11) to yield:

$$AF_{AZC}^{b_{AZ}}(r_0, r) = [AF(r_0)^{b_{AZ}}SZ(r, r_m) + AF(r_m)^{b_{AZ}}SZ(r_0, r)] / AF(r_0)^{b_{AZ}}SZ(r_0, r_m) \quad (A.4)$$

820

The corrected reflectivity profile is then derived from (2.2), (2.3), (A.3) and (A.4) to read as:

$$Z_{AZC}(r) = Z_m(r) [AF(r_0)^{b_{AZ}} - AF(r_m)^{b_{AZ}}]^{1/b_{AZ}} / \{0.46 a_{AZ} b_{AZ} [AF(r_0)^{b_{AZ}}SZ(r, r_m) + AF(r_m)^{b_{AZ}}SZ(r_0, r)]\}^{1/b_{AZ}} \quad (A.5)$$

825

Note that in the previous derivations, the expression of dC given by (A.3) is used two times, first in the expression of $AF_{AZC}^{b_{AZ}}(r_0, r)$ from (2.11) and then in the substitution of dC in (2.2).

The specific attenuation profile follows from the use of the A-Z relationship (2.5):

830

$$A_{AZC}(r) = Z_m(r)^{b_{AZ}} [AF(r_0)^{b_{AZ}} - AF(r_m)^{b_{AZ}}] / \{0.46 b_{AZ} [AF(r_0)^{b_{AZ}}SZ(r, r_m) + AF(r_m)^{b_{AZ}}SZ(r_0, r)]\} \quad (A.6)$$

A.3 AZ α algorithm (independent of a_{AZ})

835

The attenuation constraint (2.12) is used to express a_{AZ} as:

$$a_{AZ} = [dC^{b_{AZ}} (AF(r_0)^{b_{AZ}} - AF(r_m)^{b_{AZ}})] / [0.46 b_{AZ} SZ(r_0, r_m)] \quad (A.7)$$

840

which can be introduced in (2.11) to yield:

$$AF_{AZ\alpha}^{b_{AZ}}(r_0, r) = [AF(r_0)^{b_{AZ}}SZ(r, r_m) + AF(r_m)^{b_{AZ}}SZ(r_0, r)] / AF(r_0)^{b_{AZ}}SZ(r_0, r_m) \quad (A.8)$$

Mis en forme : Police : Non Italique

845 Equation A.8 is actually identical to the $AF_{AZC}^{b_{AZ}}(r_0, r)$ expression (A.4). From (A.8), (2.2) and (2.3), the resulting corrected reflectivity profile can be expressed as:

$$Z_{AZ\alpha}(r) = Z_m(r) SZ(r_0, r_m)^{1/b_{AZ}} / \{dC [AF(r_0)^{b_{AZ}} SZ(r, r_m) + AF(r_m)^{b_{AZ}} SZ(r_0, r)]\}^{1/b_{AZ}} \quad (A.9)$$

850 One can note that $Z_{AZ\alpha}(r)$ is different from $Z_{AZC}(r)$ (A.5) and that it depends on dC.

850 Next, it can be verified by using (A.9), (2.5) and (A.7) (a second time, for the necessary substitution of a_{AZ}) that the $AZ\alpha$ specific attenuation profile is identical to the AZC specific attenuation profile given by (A.6) with:

$$855 \quad A_{AZ\alpha}(r) = Z_m(r)^{b_{AZ}} [AF(r_0)^{b_{AZ}} - AF(r_m)^{b_{AZ}}] / \{0.46 b_{AZ} [AF(r_0)^{b_{AZ}} SZ(r, r_m) + AF(r_m)^{b_{AZ}} SZ(r_0, r)]\} \quad (A.10)$$

A.4 AZ0 algorithm (independent of PIA_0)

860 The attenuation constraint (2.12) is used to express $AF(r_0)^{b_{AZ}}$ as:

$$860 \quad AF(r_0)^{b_{AZ}} = [0.46 a_{AZ} b_{AZ} SZ(r_0, r_m) + (AF(r_m) dC)^{b_{AZ}}] / dC^{b_{AZ}} \quad (A.11)$$

which can be introduced in (2.11) to yield:

$$865 \quad AF_{AZ0}^{b_{AZ}}(r_0, r) = \{0.46 a_{AZ} b_{AZ} SZ(r, r_m) + AF(r_m)^{b_{AZ}} dC^{b_{AZ}}\} / \{0.46 a_{AZ} b_{AZ} SZ(r_0, r_m) + (AF(r_m) dC)^{b_{AZ}}\} \quad (A.12)$$

The resulting corrected reflectivity profile is:

$$870 \quad Z_{AZ0}(r) = Z_m(r) / \{0.46 a_{AZ} b_{AZ} SZ(r, r_m) + (AF(r_m) dC)^{b_{AZ}}\}^{1/b_{AZ}} \quad (A.13)$$

And the specific attenuation profile:

$$875 \quad A_{AZ0}(r) = a_{AZ} Z_m(r)^{b_{AZ}} / \{0.46 a_{AZ} b_{AZ} SZ(r, r_m) + (AF(r_m) dC)^{b_{AZ}}\} \quad (A.14)$$

Mis en forme : Police : +Titres (Times New Roman)

Code and data availability

There will be no problem to make available ~~at a later stage~~ the codes / data developed / used in this study, preferably through demands of collaboration to the authors.

880

Conflict of interest

The authors declare that they have no conflict of interest.

Author contribution

885 GD is the main contributor for this article (concept, theoretical developments, calculations, article writing, corresponding author). AKK (PhD student) and BB (assistant professor) are scientists contributing actively to the RadAlp experiment. They performed the internal review of the article. FC is a research engineer who built and keeps improving the XPORT radar, a key instrument deployed in the RadAlp experiment. BB is also the HMCIS team leader and as such does a lot of work for all the team members.

890

Acknowledgements

We thank the three anonymous reviewers for their valuable comments, which helped us improving the article. We are grateful to P.N. Gatlin (NASA Marshall Space Flight Center, Huntsville, AL) for providing the CANTMAT version 1.2 software developed at Colorado State University by C. Tang and V.N. Bringi, who we also thank. The RadAlp experiment is co-funded
895 by the Labex osug@2020 of the Observatoire des Sciences de l'Univers de Grenoble, the Service Central Hydrométéorologique et d'Appui à la Prévision des Inondations (SCHAPI) and Electricité de France / Division Technique Générale (EDF/DTG).

References

- 900 Beard, K.V., and Chuang, C.: A new model for the equilibrium shape of raindrops, *J. Atmos. Sci.*, 44, 1509-1524. [https://doi.org/10.1175/1520-0469\(1987\)044<1509:ANMFTE>2.0.CO;2](https://doi.org/10.1175/1520-0469(1987)044<1509:ANMFTE>2.0.CO;2), 1987.
- Bringi, V.N., and Chandrasekar, V.: *Polarimetric Doppler weather radar, principles and applications*. Cambridge University Press, 636 pp, 2001.
- 905 Delrieu, G., Caoual, S., Creutin, J.D.: Feasibility of using mountain return for the correction of ground-based X-band weather radar data. *J. Atmos. Oceanic Technol.*, 14(3), 368-385 DOI: 10.1175/1520-0426(1997)014<0368:F0UMRF>2.0.CO;2, 1997.
- 910 Delrieu, G., Serrar, S., Guardo, E., and Creutin, J.D.: Rain Measurement in Hilly Terrain with X-Band Weather Radar Systems: Accuracy of Path-Integrated Attenuation Estimates Derived from Mountain Returns. *J. Atmos. Oceanic Technol.*, 16, 405–416, [https://doi.org/10.1175/1520-0426\(1999\)016<0405:RMIHTW>2.0.CO;2](https://doi.org/10.1175/1520-0426(1999)016<0405:RMIHTW>2.0.CO;2), 1999.

- 915 Delrieu, G., Huc, L., and Creutin, J.D.: Attenuation in rain for X- and C-band weather radar systems: Sensitivity with respect to the drop size distribution. *Journal of Applied Meteorology*, *J. Appl. Meteor.*, 38(1): 57-68. [https://doi.org/10.1175/1520-0450\(1999\)038<0057:AIRFXA>2.0.CO;2](https://doi.org/10.1175/1520-0450(1999)038<0057:AIRFXA>2.0.CO;2), 1999b.
- 920 Delrieu, G., Khanal, A.K., Yu, N., Cazenave, F., Boudevillain, B., and Gaussiat, N.: Preliminary investigation of the relationship between differential phase shift and path-integrated attenuation at the X band frequency in an Alpine environment. *Atmos. Meas. Tech.*, 13, 3731–3749, <https://doi.org/10.5194/amt-13-3731-2020>, 2020
- 925 Foresti, L., Sideris, I.V., Panziera, L., Nerini, D., and Germann, U.: A 10-year radar-based analysis of orographic precipitation growth and decay patterns over the Swiss Alpine region. *Q. J. R. Meteorol. Soc.*, 144(176), 2277-2301, DOI: 10.1002/qj.3364, 2018.
- 930 Frasier, S.J., Kabeche, F., Figueras i Ventura, J., Al-Sakka, H., Tabary, P., Beck, J. and Bousquet, O.: In-place estimation of wet radome attenuation at X band. *J. Atmos. Oceanic Technol.*, 30, 917–928, <https://doi.org/10.1002/qj.3366>, 2013.
- Germann, U., Galli, G., Boscacci, M., and Bolliger, M.: Radar precipitation measurement in a mountainous region. *Q. J. Royal Meteorol. Soc.*, 132(618), 1669-1692; DOI: 10.1256/qj.05.190, 2006.
- 935 Gorgucci, E., and Chandrasekar V.: Evaluation of attenuation correction methodology for dual-polarization radars: Application to X-band systems. *J. Atmos. Oceanic Technol.*, **22**, 1195–1206, doi:10.1175/JTECH1763.1, 2005.
- 940 Haddad, Z.S., Im, E., and Durden, S.L.: Intrinsic ambiguities in the retrieval of rain rates from radar returns at attenuating wavelengths. *Journal of Applied Meteorology and J. Appl. Meteor.*, *Climatology*, 1995, vol. 34, no 12, p. 2667-2679.
- Joss, J. and Lee, R.: The Application of Radar-Gauge Comparisons to Operational Precipitation Profile Corrections. *J. Appl. Meteor.*, 34, 2612–2630, [http://dx.doi.org/10.1175/1520-0450\(1995\)034<2612:TAORCT>2.0.CO;2](http://dx.doi.org/10.1175/1520-0450(1995)034<2612:TAORCT>2.0.CO;2), 1995.
- 945 Khanal, A. K., Delrieu, G., Cazenave, F., and Boudevillain, B.: Radar remote sensing of precipitation in high mountains: detection and characterization of Melting Layer in French Alps, *Atmosphere*, 10, 784; doi:10.3390/atmos10120784, 2019.
- Khanal, A. K., Delrieu, G., Cazenave, F., and Boudevillain, B.: Investigation of the relationship between path-integrated attenuation (PIA) and differential phase shift (Φ_{dp}) in the melting layer of precipitation at X-band frequency. Submitted in preparation for submission to *Atmospheric Measurement Techniques*, January/June 2022.
- 950 Koffi, A.K., Gosset, M., Zahiri, E.-P., Ochou, A.D., Kacou, M., Cazenave, F., and Assamoi, P.: Evaluation of X-band polarimetric radar estimation of rainfall and rain drop size distribution parameters in West Africa. *Atmospheric Research*, 143, 438-461. DOI:10.1016/j.atmosres.2014.03.009, 2014.
- 955 Lengfeld, K., Clemens, M., Münster, H., and Ament, F., 2014.: Performance of high-resolution X-band weather radar networks – the PATTERN example, *Atmospheric Measurement Techniques*, *Atmos. Meas. Tech.*, 7, 4151–4166, <https://doi.org/10.5194/amt-7-4151-2014>, 2014
- Mancini, A., J. L. Salazar, R. M. Lebrón, and Cheong B. L.: A novel instrument for real-time measurement of attenuation of weather radar radome including its outer surface. Part II: the concept. *J. Atmos. Oceanic Technol.*, 35, 953–973, <https://doi.org/10.1175/JTECH-D-17-0083.1>, 2018.
- 960 Marzoug, M., and Amayenc, P.: A class of single and dual-frequency algorithms for rain-rate profiling from a spaceborne radar: Part 1- Principle and tests from numerical simulations. *J. Atmos. Oceanic Technol.*, 11, 1480-1506. [http://dx.doi.org/10.1175/1520-0426\(1994\)011%3C1480:ACOSAD%3E2.0.CO;2](http://dx.doi.org/10.1175/1520-0426(1994)011%3C1480:ACOSAD%3E2.0.CO;2), 1994.

Mis en forme : Police :Non Italique

Matrosov, S. Y., and Clark, K.A.: X-Band Polarimetric Radar Measurements of Rainfall. *J. Appl. Meteor.* 41(9): 941-952. [http://dx.doi.org/10.1175/1520-0450\(2002\)041%3C0941:XBPRMO%3E2.0.CO;2](http://dx.doi.org/10.1175/1520-0450(2002)041%3C0941:XBPRMO%3E2.0.CO;2), 2002.

965 Matrosov, S.Y., Kingsmill, D.E., Martner, B.E., and Ralph, F.M.: The Utility of X-Band Polarimetric Radar for Quantitative Estimates of Rainfall Parameters. *J. Hydrometeorol.*, 6, 248–262, <https://doi.org/10.1175/JHM424.1>, 2005.

Matrosov, S.Y., Campbell, C., Kingsmill, D.E., and Sukovich, E.: Assessing Snowfall Rates from X-Band Radar Reflectivity Measurements. *J. Atmos. Oceanic Technol.*, 26, 2324–2339, DOI: 10.1175/2009JTECHA1238.1, 2009.

970 Matrosov, S.Y., Kennedy, P.C., Cifelli, R.: Experimentally Based Estimates of Relations between X-Band Radar Signal Attenuation Characteristics and Differential Phase in Rain. *J. Atmos. Oceanic Technol.*, 31, 2442-2450. <https://doi.org/10.1175/JTECH-D-13-00231.1>, 2014.

975 Meneghini, R., J. Eckermann, and Atlas, D.: Determination of rain rate from a space borne radar using measurements of total attenuation. *IEEE Transactions in Geosciences and Remote Sensing*, GE-21, 34-43, 1983.

Meneghini, R., H. Kim, L. Liao, J. Kwiatkowski, J., and T-Iguchi, 2020; T.: Path attenuation estimates for the GPM Dual-frequency Precipitation Radar (DPR). *J. Meteor. Soc. Japan*, 99, 181–200, doi:10.2151/jmsj.2021-010, 2020.

980 McLaughlin, D., Pepyne, D., Chandrasekar, V., Philips, B., Kurose, J., Zink, M., Droegemeier, K., Cruz-Pol, S., Junyent, F., Brotzge, J., Westbrook, D., Bharadwaj, N., Wang, Y., Lyons, E., Hondl, K., Liu, Y., Knapp, E., Xue, M., Hopf, A., Kloesel, K., DeFonzo, A., Kollias, P., Brewster, K., Contreras, R., Dolan, B., Djaferis, T., Insanic, E., Frasier, S., and Carr, F., 2009: Short-Wavelength Technology and the Potential For Distributed Networks of Small Radar Systems. *Bulletin of the American Meteorological Society*, 90, 1797–1818, <https://doi.org/10.1175/2009BAMS2507.1>, 2009.

985 Park, S.-G., Maki M., Iwanami K., Bringi, V. N., and Chandrasekar, V., Maki, M., and Iwanami, K., 2005: Correction of Radar Reflectivity radar reflectivity and Differential Reflectivity differential reflectivity for Rain Attenuation rain attenuation at X Bandband, Part I: TheoreticalII: Evaluation and Empirical Basis. *Journal of Atmospheric and application. J. Atmos. Oceanic Technology Technol.*, 22, 1621–1632, <https://1633-1655.doi.org/10.1175/JTECH1803JTECH1804.1>, 2005.

Ryzhkov, A.V., Giangrande, S.E., and Schuur, T.J.: Rainfall estimation with a polarimetric prototype of WSR-88D. *J. Appl. Meteor.*, Vol. 44, Issue 4, p502-515. DOI: 10.1175/JAM2213.1, 2005.

995 Ryzhkov, A. V., Diederich, M., Zhang Pengfei, and Simmer, C.: Potential utilization of specific attenuation for rainfall estimation, mitigation of partial beam blockage and radar networking. *J. Atmos. Oceanic Technol.*, Vol. 31, p599-619. DOI: 10.1175/JTECH-D-15-00038.1, 2014.

1000 Saltikoff, E., G. Haase, L. Delobbe, N. Gaussiat, M. Martet, D. Idziorek, H. Leijnse, P. Novák, M. Lukach, and K. Stephan, 2019. OPERA the Radar Project. *Atmosphere*, 10, 320; doi:10.3390/atmos10060320.

Saxion, D. S., and Coauthors, 2011: New science for the WSR-88D: Validating the dual polarization upgrade. 27th International Conference on Interactive Information Systems Processing for Meteorology, Oceanography, and Hydrology, Jan 22-27, 2011, Seattle, WA, USA.

1005 Schneebeli, M., and Berne, A.: An Extended Kalman Filter Framework for Polarimetric X-Band Weather Radar Data Processing. *J. Atmos. Oceanic Technol.*, 29, 711–730, <https://doi.org/10.1175/JTECH-D-10-05053.1>, 2012.

1010

- Mis en forme : Lien hypertexte
- Mis en forme : Lien hypertexte
- Mis en forme : Lien hypertexte
- Mis en forme : Lien hypertexte
- Mis en forme : Lien hypertexte
- Mis en forme : Lien hypertexte
- Mis en forme : Lien hypertexte
- Mis en forme : Lien hypertexte
- Mis en forme : Lien hypertexte
- Mis en forme : Lien hypertexte
- Mis en forme : Lien hypertexte
- Mis en forme : Lien hypertexte
- Mis en forme : Lien hypertexte
- Mis en forme : Lien hypertexte
- Mis en forme : Lien hypertexte
- Mis en forme : Lien hypertexte
- Mis en forme : Lien hypertexte
- Mis en forme : Lien hypertexte
- Mis en forme : Lien hypertexte
- Mis en forme : Lien hypertexte

Scipion, D. E., R. Mott, M. Lehning, M. Schneebeli, and A. Berne (~~2013~~): Seasonal small-scale spatial variability in alpine snowfall and snow accumulation, *Water Resour. Res.*, 49, 1446–1457, doi:10.1002/wrcr.20135, [2013](#).

1015 Serafin, R. J., and J. W. Wilson, ~~2000~~: Operational weather radar in the United States: Progress and opportunity. *Bull. Amer. Meteor. Soc.*, 81, 501–518, [2000](#).

Serrar, S., Delrieu, G., Creutin, J.D., Uijlenhoet, and R.: Mountain Reference Technique: Use of mountain returns to calibrate weather radars operating at attenuating wavelengths. *J. Geophys. Res. – Atmospheres*, 105(D2): 2281-2290. DOI :10.1029/1999JD901025, 2000.

1020 Sideris, I. V., Gabella, M., Erdin, R., and Germann, U.: Real-time radar–raingauge merging using spatio-temporal co-kriging with external drift in the alpine terrain of Switzerland. *Q. J. R. Meteorol. Soc.*, 140, 1097 – 1111, DOI:10.1002/qj.2188S, 2014.

1025 Testud, J, Le Bouar, E., Obligis, E. and Ali-Mehenni, M.: The Rain Profiling Algorithm Applied to Polarimetric Weather Radar. *J. Atmos. Oceanic Technol.*, 17: 332-356. [http://dx.doi.org/10.1175/1520-0426\(2000\)017%3C0332:TRPAAT%3E2.0.CO;2](http://dx.doi.org/10.1175/1520-0426(2000)017%3C0332:TRPAAT%3E2.0.CO;2), 2000.

1030 Trömel, S., Kumjian, M.R., Ryzhkov, A.V., Simmer, C., and Diederich, M.: Backscatter differential phase – estimation and variability. *J. Appl. Meteor. Climatol.*, 52, 2529-2548, doi: 10.1175/JAMC-D-13-0124.1, 2013.

Westrelin, S., Meriaux, P., Tabary, P., and Aubert Y.: Hydrometeorological risks in Mediterranean mountainous areas - RHYTMME Project: Risk Management based on a Radar Network. ERAD 2012 7th European Conference on Radar in Meteorology and Hydrology, June 2012, Toulouse, France. 6 p., hal-01511157, 2012.

1035 Yu, N., Gaussiat, N., and Tabary, P.: Polarimetric X-band weather radars for quantitative precipitation estimation in mountainous regions. *Q. J. Royal Meteorol. Soc.*, 144(717), DOI:10.1002/qj.3366, 2018.

Mis en forme : Justifié, Interligne : 1,5 ligne

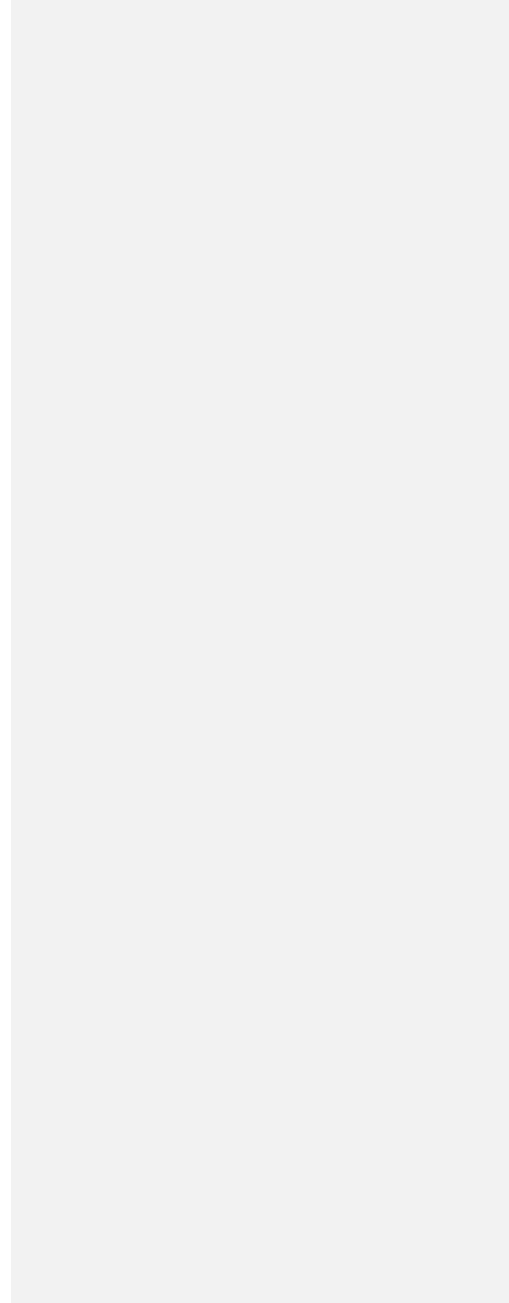


Table 1: Values and ranges of variation of the attenuation model parameters in the sensitivity analysis

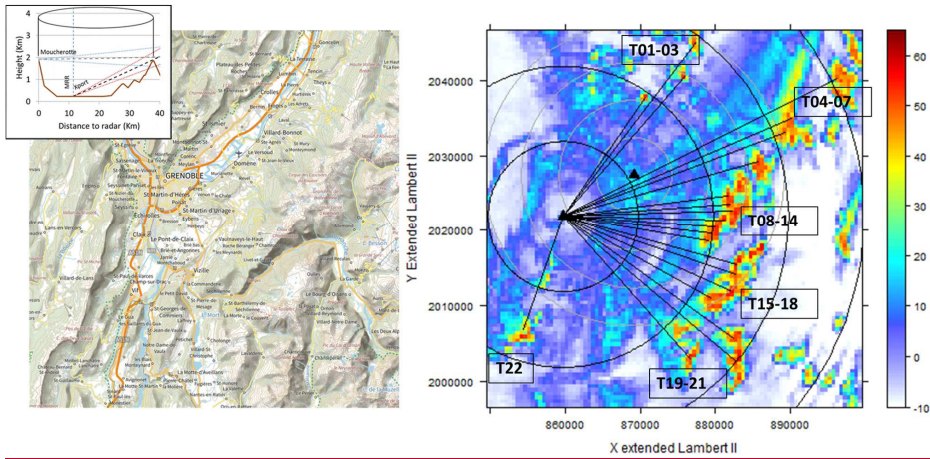
Parameters fixed for a given simulation			
Parameter	Value(s)		
$b_{\alpha Z}$	0.78		
$b_{\alpha K}$	0.9, 1.0, 1.05, 1.10, 1.15, 1.20		
dG	[-2, 2 dB] with a step of 0.4 dB		
Parameters taken into account in the Latin Hypercubes Sampling for a given simulation			
Parameter	Central value	Range of multiplicative coefficient — of — the central value (in dB)	Lower and upper limit
$\alpha_{\alpha Z}$	$1.0 \cdot 10^{-4}$	[-3, 3 dB]	$\{0.5 \cdot 10^{-4}, 2.0 \cdot 10^{-4}\}$
$\alpha_{\alpha K}$	0.3	[-3, 3 dB]	[0.15, 0.6]
dAF_{m}	1.0	[-1, 1 dB]	[0.79, 1.26]
$AF(r_0)$: sampling #1	0.316	[-5, 5 dB]	$AF(r_0)$: [1.0, 0.1] corresponding to PIA_0 : [0, 10 dB]
$AF(r_0)$: sampling #2	$PIA_0^* = 0.0126 Z_0^{1.6}$ PIA_0^* [dB]; Z_0 [dBZ] $AF^*(r_0) = 10^{-PIA_0^*/10}$		Lower limits: $PIA_0^L = 0$; $A(r_0)^L = 1$ Upper limits: $PIA_0^U = n \cdot PIA_0^*$ $A(r_0)^U = 10^{-PIA_0^U/10}$ with $n = 3$ in results of Figs 3-4; 7-8 and $n = 10$ in results of Figs. 9-10

Parameters fixed for a given simulation			
Parameter	Value(s)		
b_{AZ}	0.80		
b_{AK}	0.9, 1.0, 1.05, 1.10, 1.15, 1.20		
dC	-2, -1.25, -1, -0.75, -0.5, -0.25, 0, 0.25, 0.5, 0.75, 1, 1.25, 2		
Parameters taken into account in the Latin Hypercubes Sampling for a given simulation			
Parameter	Central value	Range of multiplicative coefficient of the central value (in dB)	Lower and upper limit
a_{AZ}	$1.0 \cdot 10^{-4}$	[-3, 3 dB]	$[0.5 \cdot 10^{-4}, 2.0 \cdot 10^{-4}]$
a_{AK}	0.3	[-3, 3 dB]	[0.15, 0.6]
dAF_m	1.0	[-1, 1 dB]	[0.79, 1.26]
$AF(r_0)$	$PIA_0^* = 0.0126 Z_0^{1.6}$ $PIA_0^* \text{ [dB]; } Z_0 \text{ [dBZ]}$ $AF^*(r_0) = 10^{-PIA_0^*/10}$		Lower limits: $PIA_0^L = 0; A(r_0)^L = 1$ Upper limits: $PIA_0^U = n PIA_0^*$ $A(r_0)^U = 10^{-PIA_0^U/10}$ with $n = 5$

050

Table 2. Some characteristics of the three convective events considered in this study. The melting layer (ML) detection was performed with the 25°-elevation angle measurements of the XPORT radar using the algorithm described in Khanal et al. (2019). The total rain amount and the maximum rainrate are recorded at the raingauge available at the IGE site at the bottom of the Grenoble valley. The PIA_m statistics are derived from the MRT by considering all the 22 mountain targets and the 0° elevation data of the Moucherotte Mount radar.

Date	Beginning (UTC)	End (UTC)	Minimum altitude of the ML bottom (m asl)	Total rain amount (mm)	Maximum rainrate in 10 min (mm h ⁻¹)	Maximum PIA_m value (dB)	Number of profiles with PIA_m greater than a given value
21 July 2017	15:30	19:00	3000	35.2	42.0	59.8	11 (> 40 dB)
8 August 2017	8:30	14:00	3700	27.9	48.0	63.4	20 (> 40 dB)
31 August 2017	7:00	11:30	3200	19.9	15.5	17.5	8 (> 15 dB)



Date	Beginning (UTC)	End (UTC)	Figure 1: Left - 50x50 km² map of the region of Grenoble, France (from Geoportail, Institut Géographique National); Right - Dry-weather reflectivity map of the X-Band weather radar located on top of the Moucherotte Mount (1901 m asl)	Total rainfall amount (mm)	Maximum rainfall rate in 10 min (mm h ⁻¹)	Maximum PIA ₁₀₀ value (dB)	Number of profiles with PIA ₁₀₀ greater than a given value

- Cellules supprimées
- Cellules supprimées
- Cellules supprimées
- Cellules supprimées
- Tableau mis en forme
- Cellules supprimées
- Cellules supprimées
- Cellules supprimées

in the Vercors
massif. The radar is
marked with a black
triangle and circular
range markers
spaced by 10 km.
The Cartesian map
has a resolution of
500 m. The
measurements were
taken at an elevation
angle of 0° during
dry-weather
conditions before the
21 July 2017 event.
The radial lines
indicate the azimuths
and ranges of the 22
mountain targets
used for the MRT
implementation.
Targets 1-3 are
located in the
Chartreuse Massif,
targets 4-14 in the
Belledonne Massif,
targets 15-21 in the
Taillefer Massif and
Target 22 in the
Vercors Massif.
Minimum altitude of
the ML bottom
(m asb)In the
background, the

second black triangle indicates the IGE site at the bottom of the valley (210 m asl). The grey circles with 5 km spacing indicate the coverage of the XPORT X-Band polarimetric radar whose measurements were used in the present study only for the detection of the melting layer.

21 July 2017	15:30	19:00	3000	35.2	42.0	59.8	11 (\Rightarrow 40 dB)
8 August 2017	8:30	14:00	3700	27.9	48.0	63.4	20 (\Rightarrow 40 dB)
31 August 2017	7:00	11:30	3200	19.9	15.5	17.5	8 (\Rightarrow 15 dB)

Mis en forme : Gauche, Interligne : simple

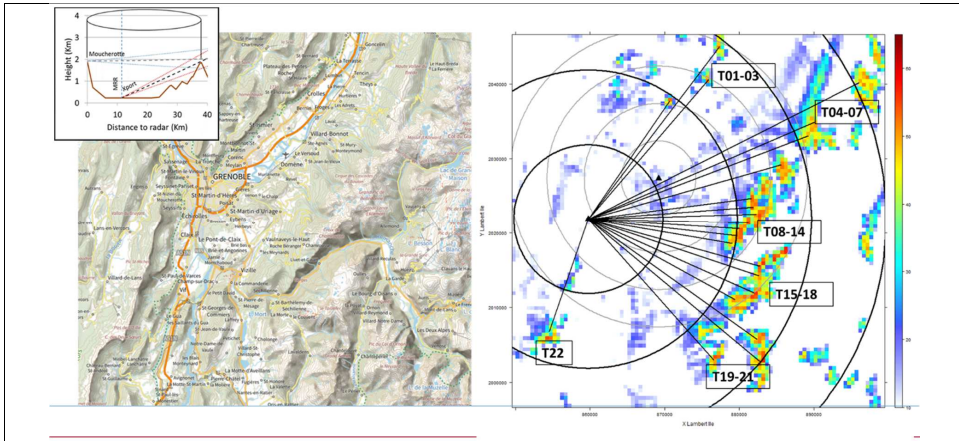
Mis en forme : Interligne : 1,5 ligne

1075

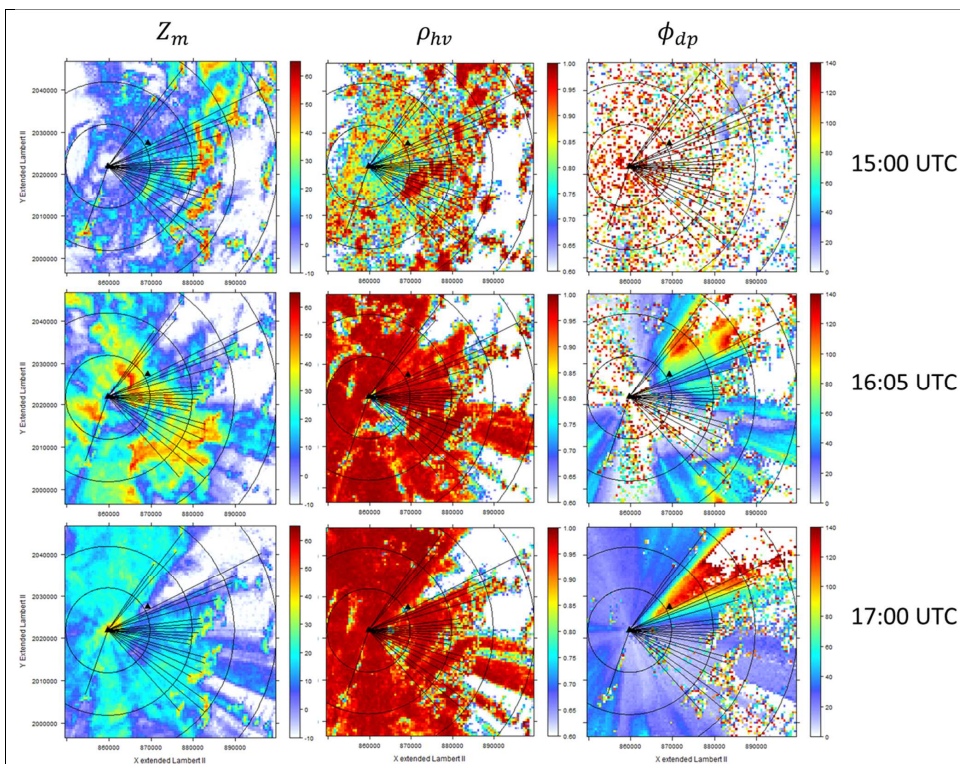
1080

085

Mis en forme : Gauche, Interligne : simple



Mis en forme : Interligne : simple

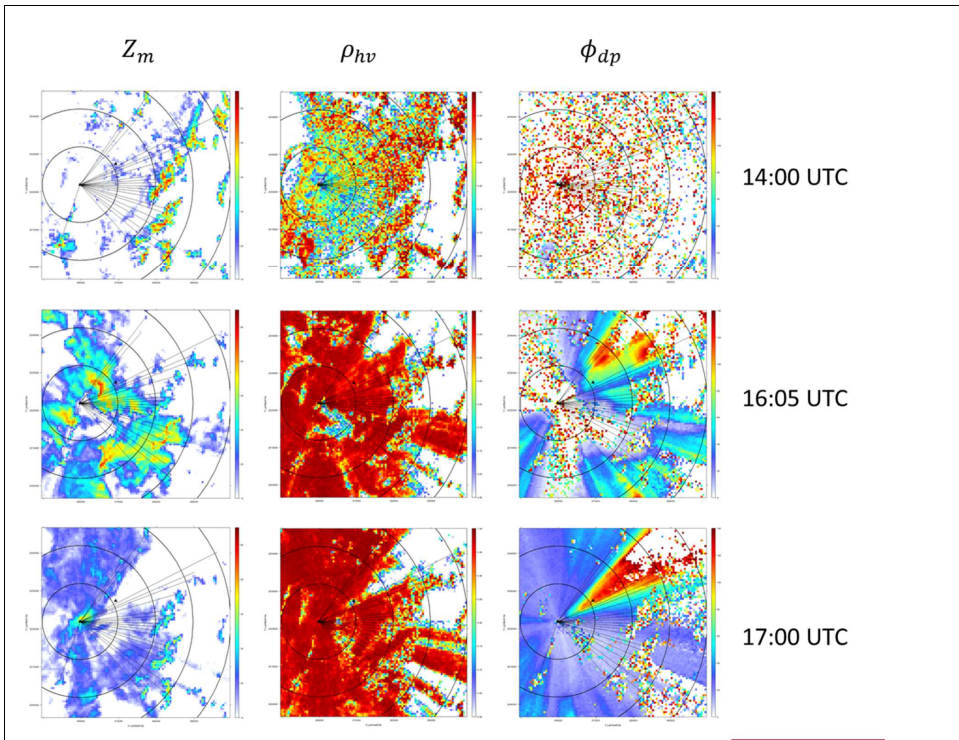


Mis en forme : Anglais (Royaume-Uni)

Figure 2: Examples of 0° -elevation PPIs of measured reflectivity (left), co-polar correlation coefficient (middle) and total differential phase shift (right) taken before (top) and at two moments with intense precipitation (middle and bottom) during the 21 July 2017 convective event. As in Fig. 1, the circular range markers of the Moucherotte Mount radar are spaced by 10 km. **Figure 1:** Left— $50 \times 50 \text{ km}^2$ map of the region of Grenoble, France (from Geoportail, Institut Géographique National); Right—Reflectivity map of the X-Band weather radar located on top of the Moucherotte Mount (1901 m asl) in the Vercors massif. The radar is marked with a black triangle and circular range markers spaced by 10 km. The Cartesian map has a resolution of 500 m. The measurements were taken at an elevation angle of 0° during dry weather conditions before the 21 July 2017 event. The radial lines indicate the azimuths and ranges of the 22 mountain targets used for the MRT implementation. Targets 1-3 are located in the Chartreuse Massif, targets 4-14 in the Belledonne Massif, targets 15-21 in the Taillefer Massif and Target 22 in the Vercors Massif. In the background, the black triangle indicates the IGE site at the bottom of the valley (210 m asl). The grey circles with 5 km spacing indicate the coverage of the XPORT X-Band polarimetric radar whose measurements were used in the present study only for the detection of the melting layer.

Mis en forme : Gauche, Interligne : simple

Mis en forme : Interligne : 1,5 ligne



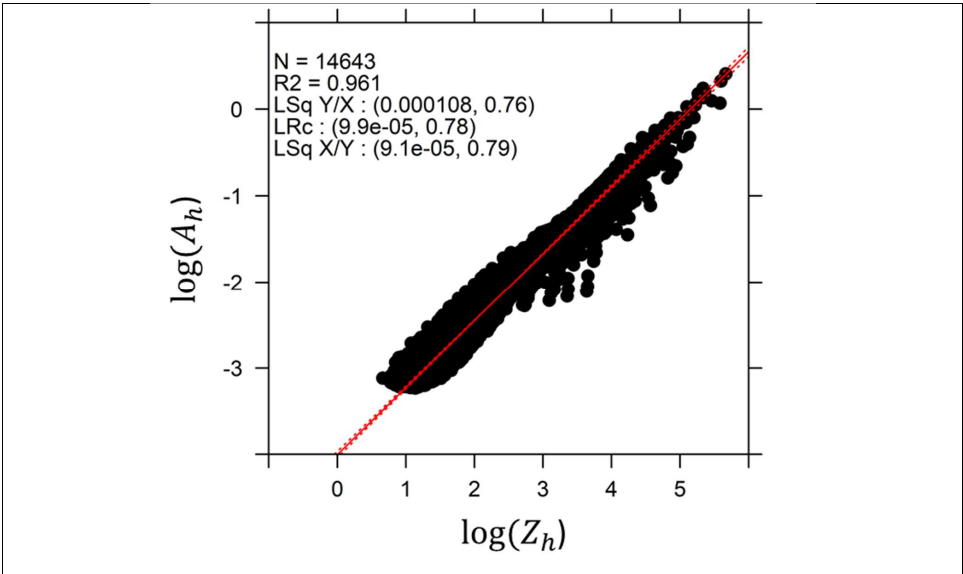


Figure 3: Results of the fitting of DSD-derived power-law models for the horizontal specific attenuation A_h [dB km⁻¹] as a function of the horizontal reflectivity Z_h [mm⁶ m⁻³] using a classical logarithmic of base 10 transformation of the two variables. Are given in the insert the number of points N , the square of the correlation coefficient (R^2) of the logarithmic regression, the prefactors and exponents of the resulting least-square regressions of the variable in ordinate versus the variable in abscissa (LSq Y/X) and vice versa (LSq X/Y) as well as the least-rectangle regression (LRc) which considers the two variables on an equal footing.

Figure 2: Examples of 0° elevation PPIs of measured reflectivity (left), co-polar correlation coefficient (middle) and total differential phase shift (right) taken before (top) and at two moments of intense precipitation (middle and bottom) during the 21 July 2017 convective event.

As in Fig. 1, the circular range markers of the Moucheroite Mount radar are spaced by 10 km.

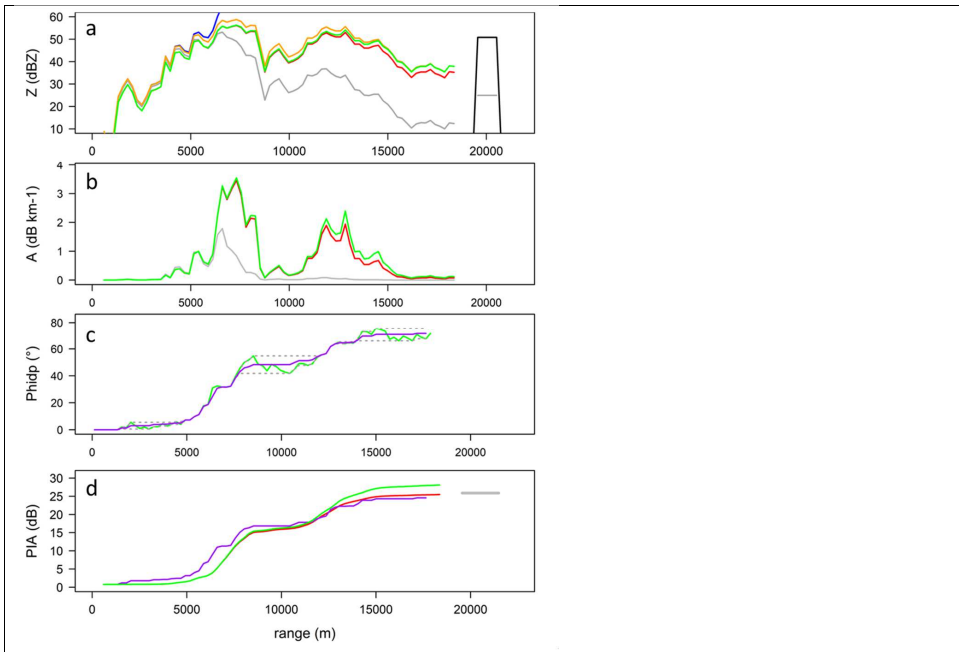
Mis en forme : Police :Non Italique

Mis en forme : Police :Non Italique

Mis en forme : Police :Non Italique

Mis en forme : Police :Non Italique

Mis en forme : Police :Non Italique



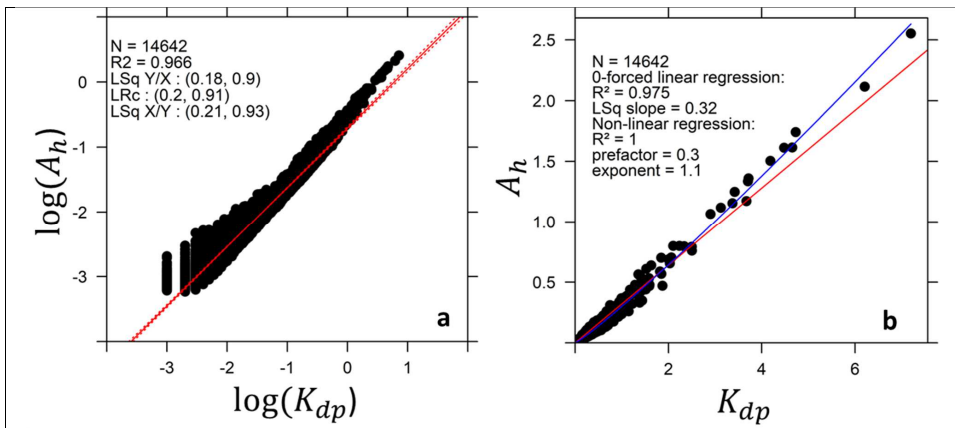


Figure 4: Fitting of DSD-derived power-law models for the horizontal specific attenuation A_h [dB km^{-1}] as a function of the specific differential phase shift on propagation K_{dp} [$^{\circ} \text{km}^{-1}$] (a) using a classical logarithmic of base 10 transformation of the two variables (same comments as in Fig. Figure 3: Implementation of the five algorithms (blue: AZhb; red: AZC; orange: AZa; green: AZ0; purple: PIA_{app}^3 for this graph) and (b) using natural values of the two variables. The red line in (b) is the 0-forced linear regression with a slope equal to 0.32 and the blue curve is the non-linear fit of a power-law model with a prefactor of 0.30 and an exponent of 1.1.

) for mountain target T13 during the 21 July 2017 convective event at 16:00 UTC using a near-optimal parameter set (see text for details). The results are displayed in terms of profiles of (a) reflectivity, (b) specific attenuation, (c) differential phase shift on propagation and (d) path-integrated attenuation. The grey profile in (a) is the measured reflectivity profile; the black and grey horizontal lines at range 20 km represent the mean dry-weather baseline and current reflectivities, respectively, of the mountain target. The resulting measured PIA value of 25.2 dB is reported in grey in (d). The grey profile in (b) is derived from the measured reflectivity profile by using eq. 2.5. The black line in (c) is the raw total differential phase shift profile and the grey dotted lines are the envelope curves used in the regularization procedure (Delrieu et al. 2020, Khanal et al. 2022).

Mis en forme : Police :Non Gras

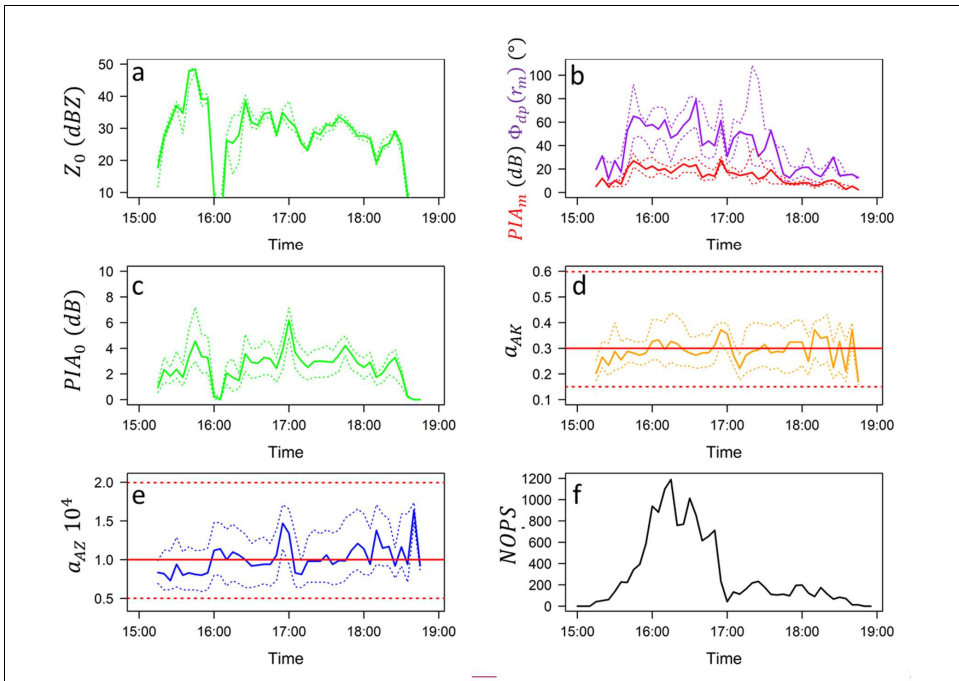
Mis en forme : Gauche

Mis en forme : Police :Non Gras

Mis en forme : Police :Non Gras

Mis en forme : Police :Non Gras

Mis en forme : Police :Non Gras



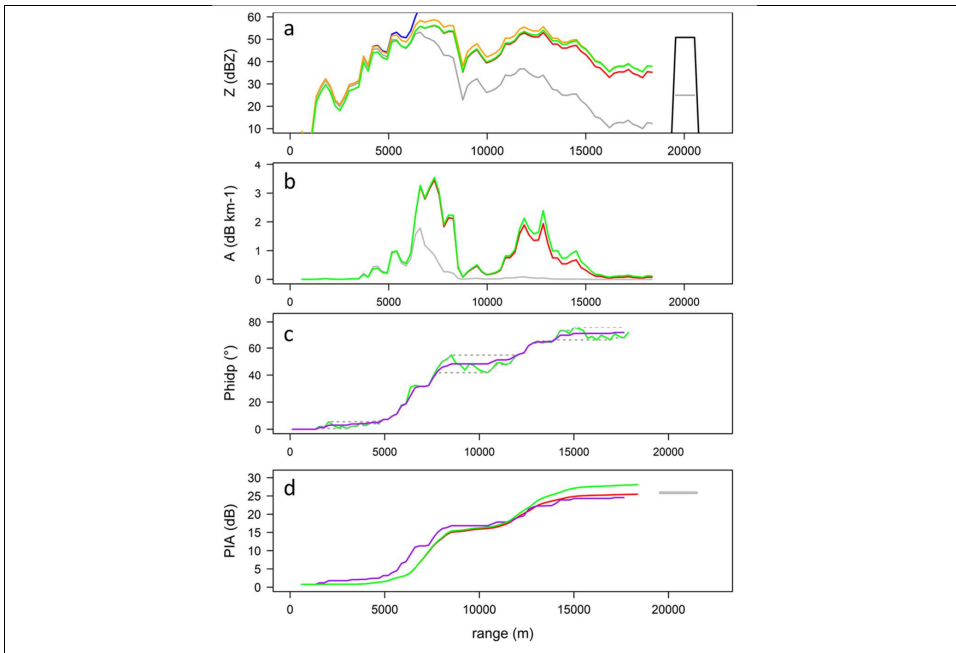


Figure 5: Implementation of the five algorithms (blue: AZhb; red: AZC; orange: AZ α ; green: AZ0; purple: PIA $_{\text{dp}}$) for mountain target T13 during the 21 July 2017 convective event at 16:00 UTC using a near-optimal parameter set (see text for details). The results are displayed in terms of profiles of (a) reflectivity, (b) specific attenuation, (c) differential phase shift on propagation and (d) path-integrated attenuation. The grey profile in (a) is the measured reflectivity profile; the black and grey horizontal lines at range 20 km represent the mean dry-weather baseline and current reflectivities, respectively, of the mountain target. The resulting measured PIA value of 25.2 dB is reported in grey in (d). The grey profile in (b) is derived from the measured reflectivity profile by using eq. 2.5. The purple line in (c) is the raw total differential phase shift profile and the grey dotted curves are the envelope curves used in the regularization procedure (Delrieu et al. 2020, Khanal et al. 2022). **Figure 4:** Time series of the input variables and optimal parameters for the best simulation obtained for the 21 July 2017 convective event. The optimal set of fixed parameters for this event is $dC^* = -0.4$ dB, $b_{AZ} = 0.78$ and $b_{AZ}^* = 1.1$. For each of the three considered input variables (a) Z_{d} ; (b) PIA_{m} (red) and $\Phi_{\text{dp}}(r_{\text{m}})$ (purple), are displayed the median (continuous line) and the 25 and 75% quantiles (dotted lines) of their distributions over the 22 mountain targets. A similar representation is proposed for the LHS optimal parameters (e) PIA_{v} ; (d) α_{AZ} ; (e) α_{AZ} , except that the distributions are established over all optimal parameters of all targets. The second sampling strategy making use of Z_{v} (see Table 1) is considered for PIA_{v} in this example. In (d) and (e), the dotted horizontal lines materialize the lower and upper limits considered in the LHS of the considered parameter. The time series of the number of optimal parameter-sets cumulated over all the 22 targets (NOPS) is displayed in (f).

Mis en forme : Centré

Mis en forme : Police : Non Gras

Mis en forme : Police : Non Gras

Mis en forme : Police : Non Gras

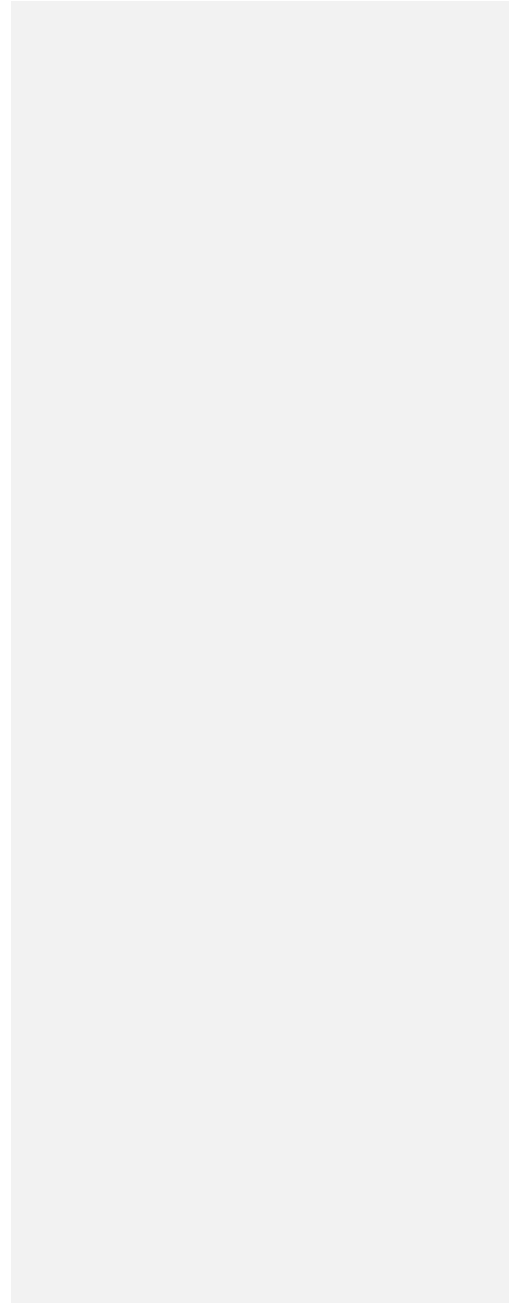
Mis en forme : Police : Non Gras

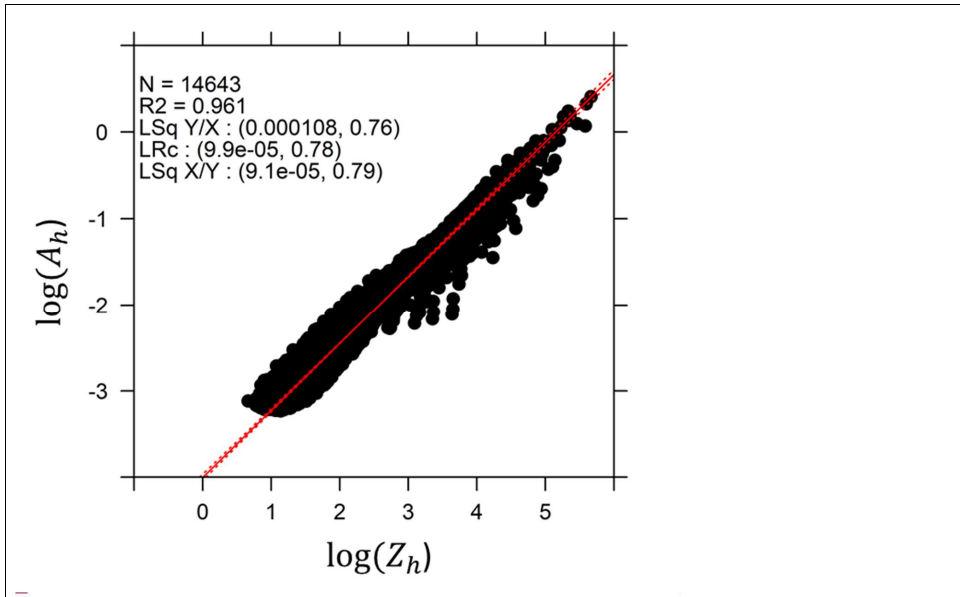
Mis en forme : Police : Non Gras

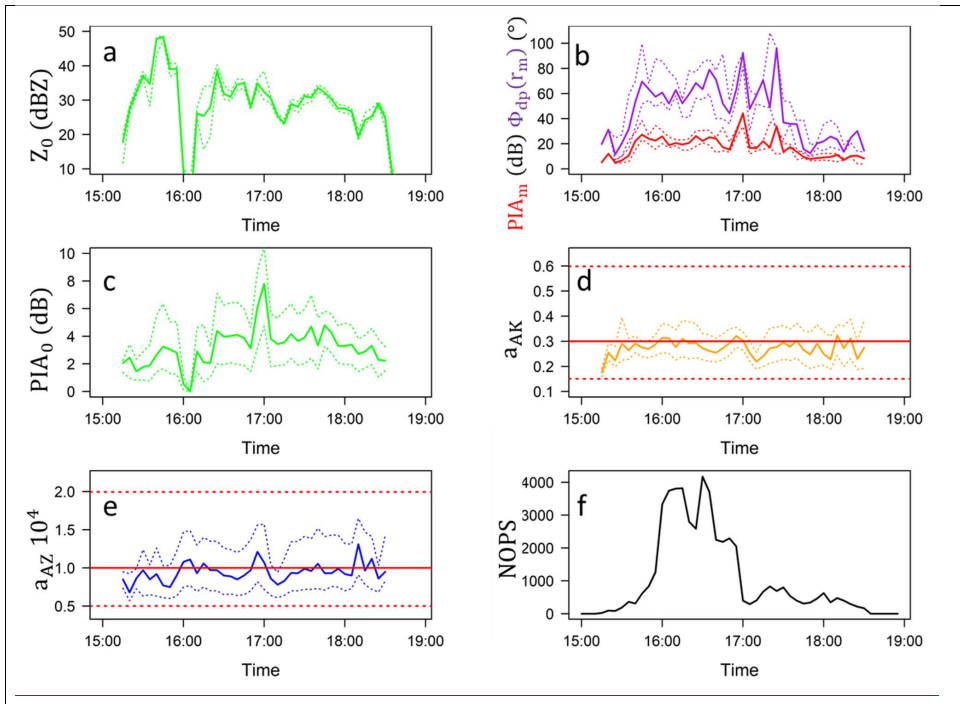
Mis en forme : Police : Non Gras

Mis en forme : Police : Non Italique

Mis en forme : Justifié







Mis en forme : Gauche

Figure 6: Time series of the input variables and optimal parameters for the best simulation obtained for the 21 July 2017 convective event. The optimal set of fixed parameters for this event is $dC = 0.5$ dB, $b_{AZ} = 0.80$ and $b_{AK} = 1.1$. For each of the three considered input variables (a) Z_0 , (b) PIA_m (red) and $\Phi_{dp}(r_0, r_m)$ (purple), are displayed the median (continuous line) and the 25 and 75% quantiles (dotted lines) of their distributions over the 22 mountain targets. A similar representation is proposed for the LHS optimal parameters (c) PIA_0 , (d) a_{AK} and (e) a_{AZ} , except that the distributions are established over all optimal parameters of all targets. In (d) and (e), the dotted horizontal lines materialize the lower and upper limits consider in the LHS of the considered parameter. **Figure 5:** Results of the fitting of DSD derived power-law models for the horizontal specific attenuation A_h [$dB km^{-1}$] as a function of the horizontal reflectivity Z_h . The time series of the number of optimal parameter sets (NOPS) cumulated over all the 22 targets is displayed in (f).

[$mm^6 m^{-3}$] using a classical logarithmic of base 10 transformation of the two variables. Are given in the insert the number of points N , the square of the correlation coefficient (R^2) of the logarithmic regression, the prefactors and exponents of the resulting least-square regressions of the variable in ordinate versus the variable in abscissa ($Log Y/X$) and vice versa ($Log X/Y$) as well as the least-rectangle regression (LRe) which considers the two variables on an equal footing.

Mis en forme : Police : Non Gras

Mis en forme : Police : Non Gras

Mis en forme : Police : Non Italique

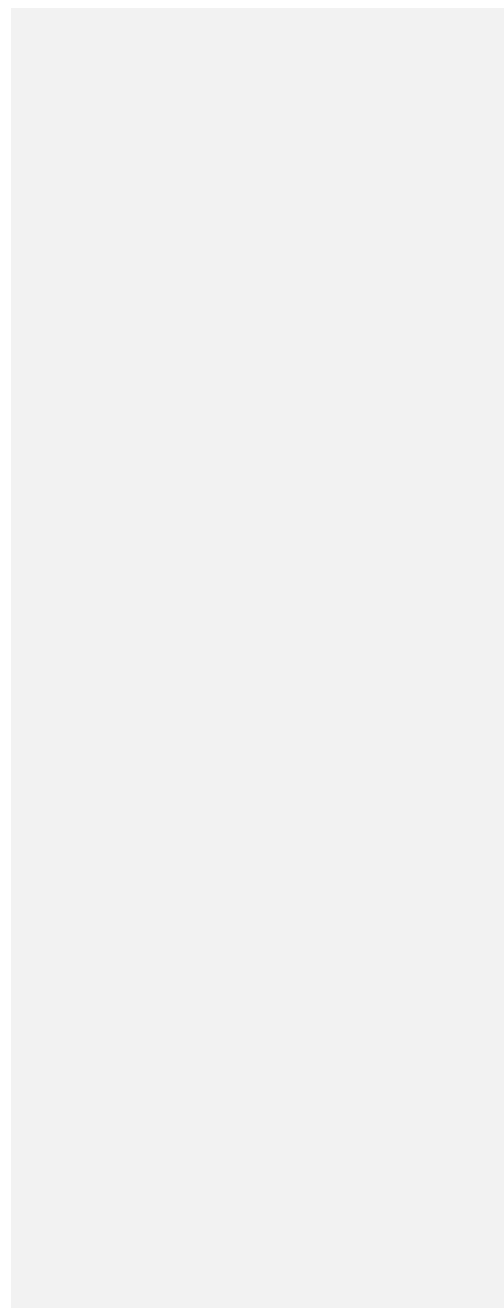
Mis en forme : Police : Non Italique

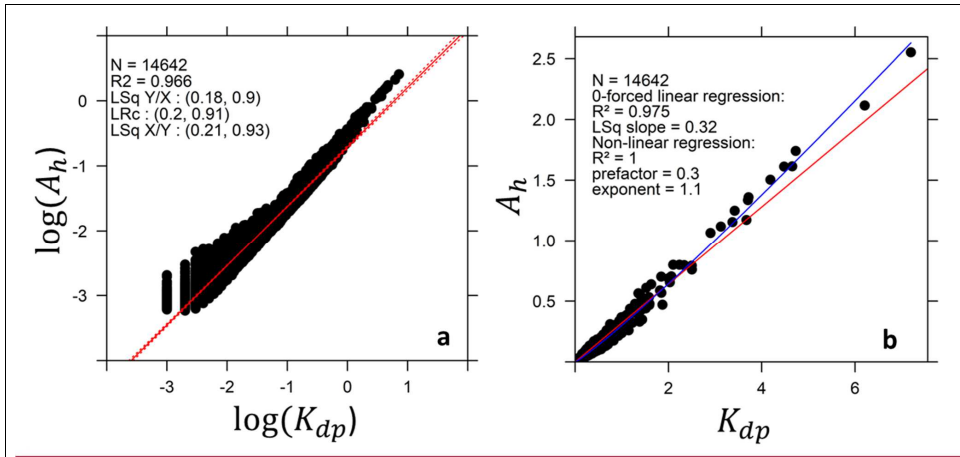
Mis en forme : Police : Non Italique

Mis en forme : Police : Non Italique

Mis en forme : Police : Non Italique

Mis en forme : Police : Non Italique





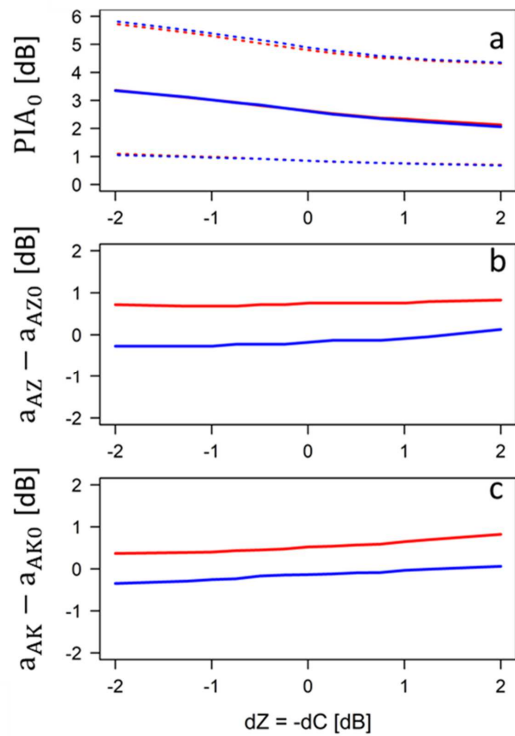
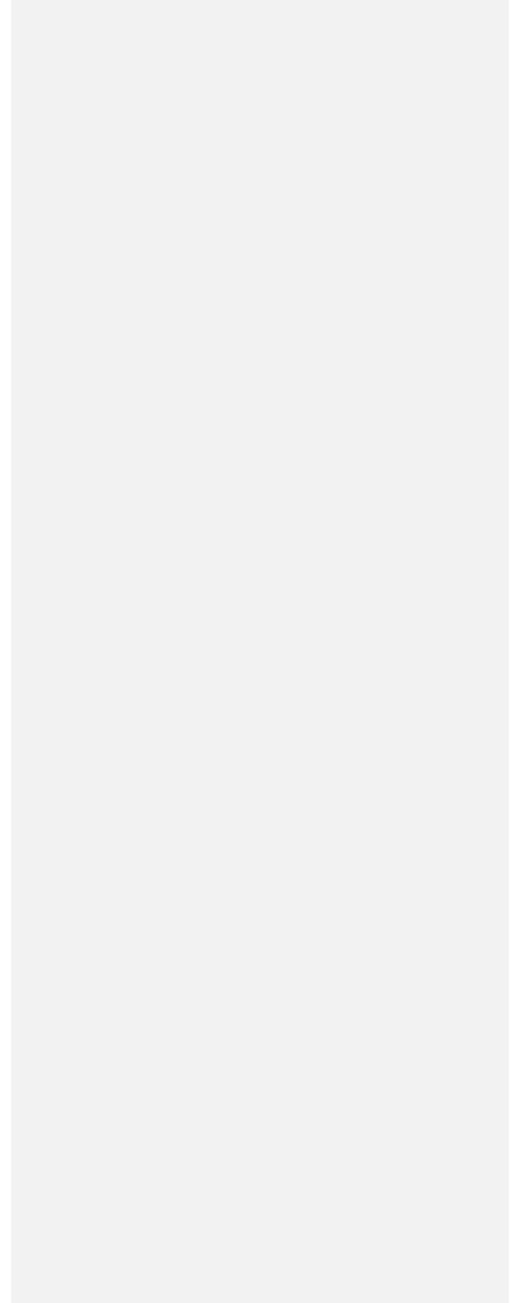


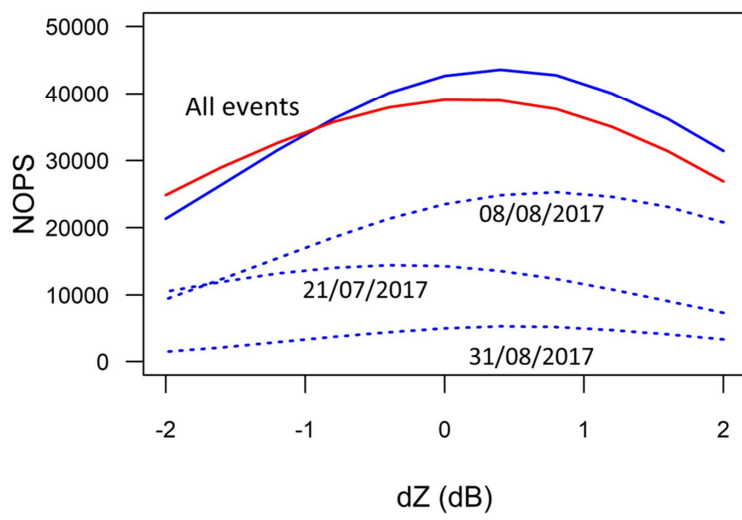
Figure 6: Fitting of DSD-derived power-law models for the horizontal specific attenuation A_h [dB km^{-1}] as a function of the specific differential phase shift on propagation K_{dp}

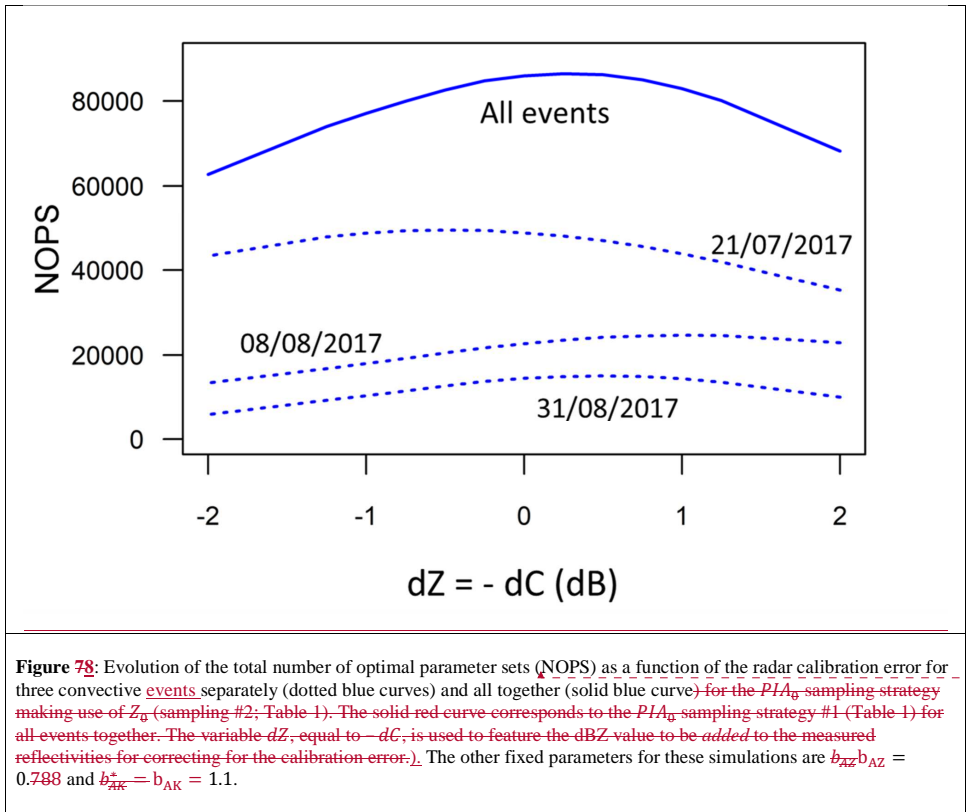
Figure 7: Evolution of the medians of the distributions of on-site attenuation (a), prefactor of the A-Z relationship (b) and prefactor of the A - K_{dp} relationship (c) estimated for the 21 July 2017 event as a function of the calibration error. The variable dZ , equal to $-dC$, is used to represent the dBZ value to be added to the measured reflectivities for correcting the calibration error. The prefactors, expressed in dB, are calculated with respect to the central values of their intervals of variation: $a_{AZ0} = 10 \log(1.0 \cdot 10^{-4})$ and $a_{AK0} = 10 \log(0.3)$ (Table 1). Like in Fig. 4b, the red curves correspond to $b_{AK} = 1$ and the blue curves to $b_{AK} = 1.1$. The dotted red and blue curves in the top graphs represent the 25 and 75% quantiles of the distributions of PIA_0 .

(km^{-1}) (a) using a classical logarithmic of base 10 transformation of the two variables (same comments as in Fig. 4 for this graph) and (b) using natural values of the two variables. The red line in (b) is the 0 forced linear regression with a slope equal to 0.32 and the blue curve is the non-linear fit of a power-law model with a prefactor of 0.30 and an exponent of 1.1.

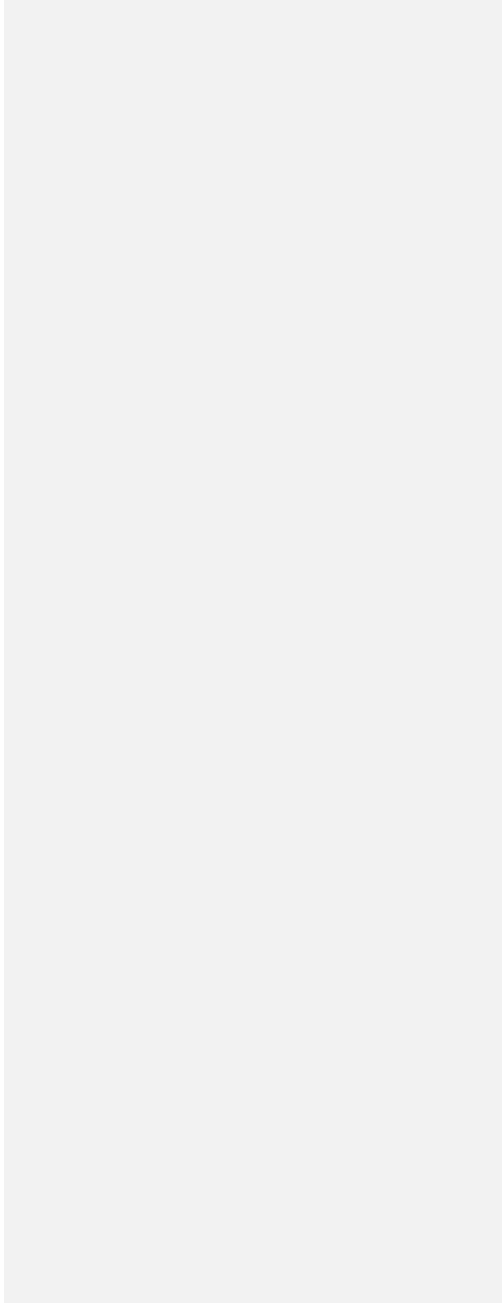
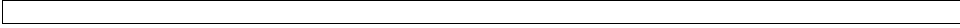
Mis en forme : Police :Non Gras

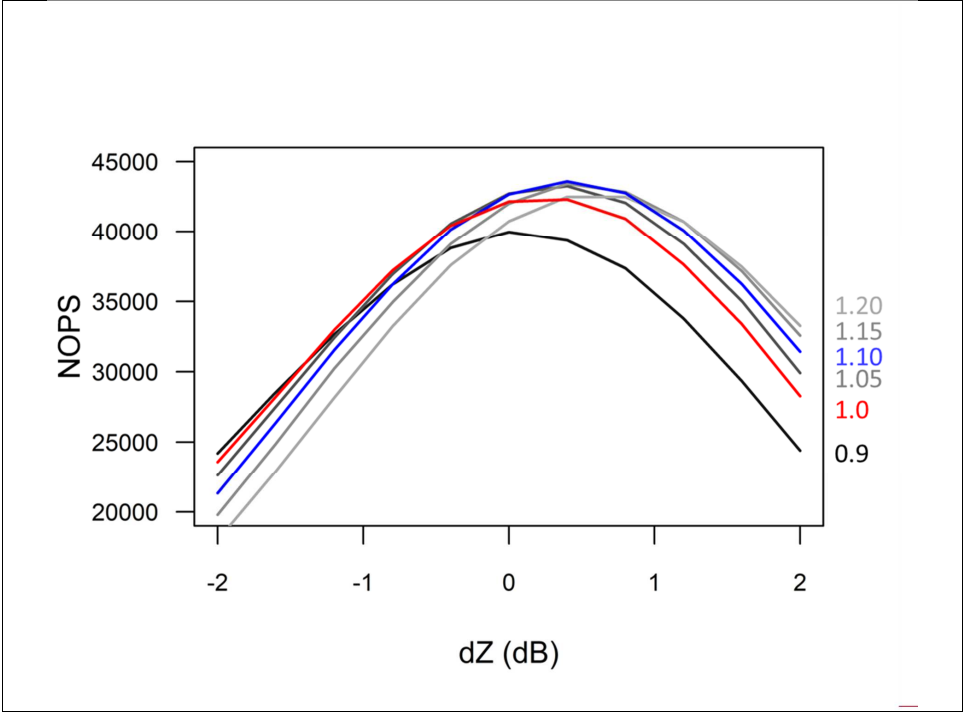






Mis en forme : Police :Non Italique





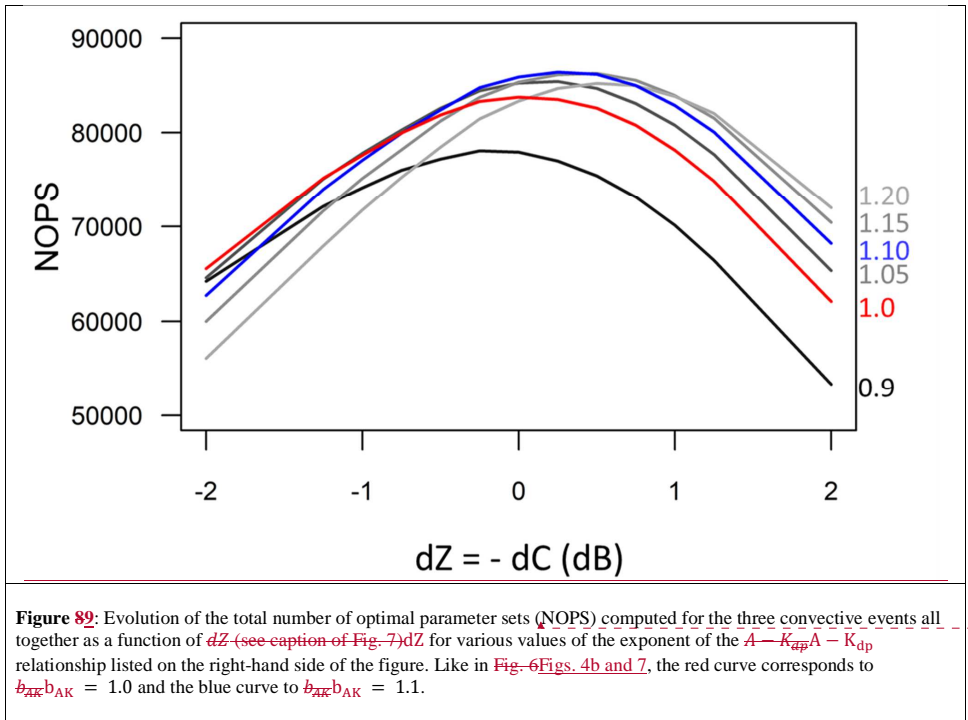
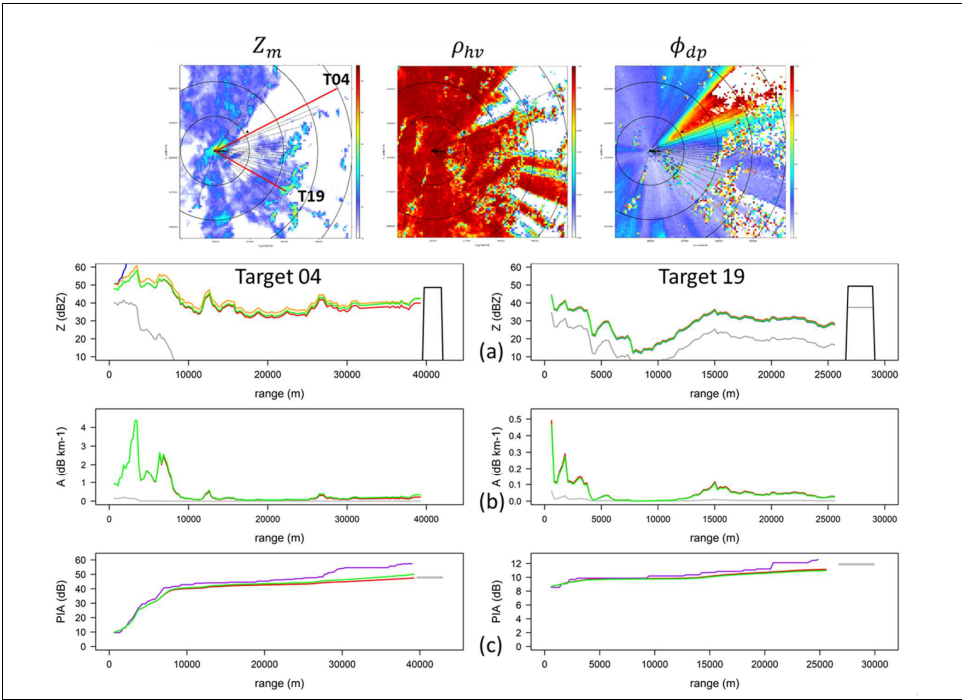


Figure 89: Evolution of the total number of optimal parameter sets (NOPS) computed for the three convective events all together as a function of dZ (see caption of Fig. 7) for various values of the exponent of the $A - K_{dp} A - K_{dp}$ relationship listed on the right-hand side of the figure. Like in Fig. 6 Figs. 4b and 7, the red curve corresponds to $b_{AK} = 1.0$ and the blue curve to $b_{AK} = 1.1$.

Mis en forme : Police :Non Italique



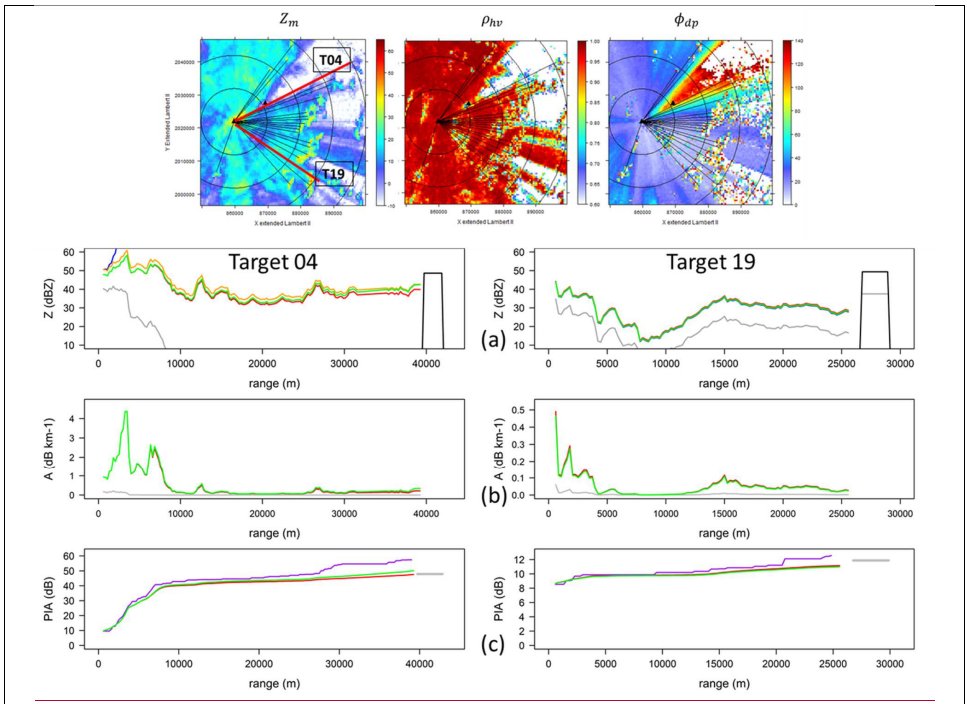


Figure 910: Implementation of the five algorithms with sets of optimal parameters (blue: AZhb; red: AZC; orange: AZ α ; green: AZ0; purple: PIA $_{\phi_{DP}}$) on 21 July 2017 at 17:00 UTC for mountain target T04 with both along-path and on-site attenuation (left), as well as for mountain target T19 with on-site attenuation mainly (right). The results are displayed in terms of profiles of (a) reflectivity, (b) specific attenuation, (c) path-integrated attenuation. In the upper images are displayed the PPIs of the measured reflectivity (with the indication of the position of the two targets in red), the co-polar correlation coefficient and the raw total differential phase shift.

Mis en forme : Police :Non Italique

Mis en forme : Police :Non Italique

Mis en forme : Police :Non Italique

Mis en forme : Police :Non Gras

Mis en forme : Police :Non Gras

Mis en forme : Police :Non Gras